This is to certify that the

thesis entitled

FRACTURE TOUGHNESS AS A FUNCTION OF PRE-EXISTING
MICROCRACKS IN YTTRIUM CHROMITE

presented by

TAE-GYO SUH

has been accepted towards fulfillment
of the requirements for

M.S. degree in Materials Science

Eldon D. Case
Major professor

Date 5/20/88

O-7639 *MSU is an Affirmative Action/Equal Opportunity Institution*

FRACTURE TOUGHNESS AS A FUNCTION OF PRE-EXISTING MICROCRACKS IN YTTRIUM CHROMITE

By

TAE-GYO SUH

A THESIS

Submitted to
Michigan State University
in partial fulfillment of the requirements
for the degree of

MASTER OF SCIENCE

Department of Metallurgy, Mechanics and Materials Science

1988

ABSTRACT

FRACTURE TOUGHNESS AS A FUNCTION OF PRE-EXISTING MICROCRACKS IN YTTRIUM CHROMITE

BY

TAE-GYO SUH

The fracture toughness and hardness of polycrystalline yttrium chromite was experimentally measured as a function of microcrack density parameter of pre-existing microcracks.

Elasticity measurements were performed by the sonic resonance technique. The microcrack density parameters were determined by the microcrack-elastic modulus theories from elastic moduli of nonmicrocracked and microcracked polycrystalline yttrium chromite. Fracture toughness and hardness were determined from the Vickers indentation technique.

Fracture toughness of polycrystalline yttrium chromite decreased linearly with microcrack density parameter. Fracture toughness changed as a function of microcrack density parameter in a fashion that seems consistent with microcrack link-up. Hardness decreased linearly with increasing the microcrack density parameter.

ACKNOWLEDGEMENTS

I wish to express my deep gratitude to Dr. Eldon D. Case for his advise and guidance in this study. I would like to thank the Division of Engineering Research for providing the funds for this research.

I should express my sincere gratitude to my parents for their encouragement and support. Finally I would like to thank my wife for her understanding and encourgement, my brother and sisters for their encouragement.

TABLE OF CONTENTS

LIST OF TABLES

LIST OF FIGURES

1. INTRODUCTION

Polycrystalline ceramic materials often exhibit excellent refractory properties and resistance to chemical corrosion, but the brittle nature of ceramics can lead to catastrophic failure under thermal or mechanical loading. For many ceramics, the increase in fracture toughness means an improved chance of producing viable components with the materials. Hence considerable research effort has been devoted to identifying and understanding physical mechanisms that increase K_c, the fracture toughness (also called the critical stress intensity factor), which is a measure of the resistance to crack growth.

One mechanism for increasing fracture toughness is crack shielding. In the crack shielding process, the microstructure of the specimen is locally altered by the crack tip stress, which in turn changes the crack tip stress field, effectively shielding the crack for the applied loading [1]. Two examples of crack shielding mechanisms are martensitic transformation and stress induced microcrack zone toughening [2,3]. Grains in a polycrystalline ceramic undergo a martensitic transformation under the influence of localized crack tip stress fields [4-10]. However, toughening of ceramics by martensitic transformation is limited, since the requisite martensitic transformation has been documented only for ZrO_2 [2-7] and HfO_2 [9,10] with some limited evidence that cordierite also may transform martensitically [10]. For the development of a stress induced microcrack zone, localized stresses (on the scale of the grain size) must be present, such as those induced by thermal expansion mismatch in anisotropic ceramics [11-13].

In addition to crack shielding mechanisms, ceramics may be toughened by a variety of crack interaction mechanisms, in which a moving crack may interact directly with preexisting microstructural features such as second phases or voids, where the increase in toughness results from crack pinning or deflection by the second phase particles [14-17].

A moving crack also may interact with pre-existing microcracks. The interaction of a moving crack and a population of pre-existing microcracks may be viewed in terms of the following two limiting cases. First, microcracks could "link-up" ahead of the propagating crack, dropping the fracture toughness by decreasing the fracture surface area formed by the moving crack. This might be case if 1) the microcracks were highly oriented, so that vectors drawn normal to the microcrack planes point in a single direction, and 2) the plane of the moving crack was coincident with the microcracks. Second, microcracks ahead of the moving crack might produce multiple crack branching. In this case, the fracture toughness could increase due to the contribution of the small, branching cracks splitting off the moving macrocrack. This might occur if each of the preexisting microcracks was oriented favorably for crack branching (perhaps, for example, with the microcracks aligned approximately normal to the plane of the moving crack). In practice, one would expect a polycrystalline ceramic to exhibt both microcrack link-up and microcrack induced branching.

Residual stress fields existing near the tips of stationary macrocracks tend to deflect the path of a moving crack away from the tip of a nearly coplanar stationary crack [18]. A similar crack deflection mechanism presumably would be operative for stationary microcracks, but due to the size of the microcrack in ceramics (often microcrack radii are of the order of the grain size [19]) direct observation of this deflection mechanism would be experimentally difficult. Nevertheless, the existence of a residual stress field near microcracks [6] and the existence of a crack deflection mechanism for stationary moving macrocrack pairs would indicate that such a mechanism ought to be considered.

Both the crack deflection mechanism (that results from residual stress fields) and the random orientation of microcracks would act to suppress microcrack link-up. Thus a population of pre-existing microcracks may increase the fracture toughness of a polycrystalline ceramic by the enhancement of crack branching.

In order to study the effect of the pre-existing microcracks upon fracture toughness, one needs a ceramic system in which the number of preexisting microcracks can be varied in a systematic manner while other microstructural features such as grain size and void size are unchanged. For ceramics that microcrack due to thermal expansion anisotropy (TEA) [11-13], the microcrack number density is a function of grain size. In order to increase the microcrack number density in a ceramic that cracks due to TEA, one can increase the grain size by annealing. However, a grain growth anneal not only changes the grain size and morphology, but also changes the void size, shape, and void fraction, along with factors that affect grain boundary strength, such as solute segregation [20].

$YCrO_3$ is, apparently, one ceramic material that can serve as an appropriate model material in this study. Yttrium chromite is an orthorhombic perovskite at room temperature. Yttrium chromite can be sintered from powders at a sufficiently high temperature in a environment with a low oxygen partial pressure. The low oxygen partial pressure is required to prevent the volatilization of chromia during sintering (For example, specimens prepared for this study were sintered in flowing forming gas at 1750°C.). Upon cooling, yttrium chromite undergoes a phase transition at 1100°C which induces microcracking. By annealing at a temperature lower than 1100°C, the microcracks can be healed, as confirmed by elasticity and small angle neutron scattering studies [19,21]. However, a subsequent thermal anneal above 1100°C can induce microcracking again. Also, it has been shown recently that the microcrack number density in polycrystalline yttrium chromite can be varied without altering other microstructural features such as the porosity and the grain size [19,21,22]. Therefore, these properties in yttrium chromite make it an excellent model material for studying the change in a material parameter, such as fracture toughness, as a function of the microcrack damage level.

The goal of this study is to determine the effect, if any, of pre-existing microcracks on the fracture toughness and hardness of polycrystalline yttrium chromite. In order to determine the level of microcrack damage, measurements of elastic moduli were related to microcrack parameters via known microcracking-elastic modulus theories. The fracture toughness of the polycrystalline yttrium chromite specimens also was measured as a function of the microcrack damage level.

Elasticity measurements were performed by the sonic resonance technique. The microcrack density parameter of the specimens was determined using equations (14) and (16) of microcrack-elastic modulus theories in Theoretical Review from Young's modulus for microcracked material, Young's modulus and Poisson's ratio for nonmicrocracked material.

Fracture toughness was determined from the Vickers indentation technique. A pyramidal shaped indentation impression was formed in the specimen by a pyramid shaped diamond. Impression size and crack size relate to hardness and fracture toughness, respectively. Hardness was computed using equation (6) in Experimental Procedure from peak indentation load and impression size. Fracture toughness was computed by using equation (7) from Young's modulus and hardness of the specimens, the peak indentation load, and the post-indentation crack length.

Briefly, this study found that the fracture toughness of polycrystalline yttrium chromite decreased linearly with ϵ, the crack density parameter. Fracture toughness changed as a function of crack density parameter changed in a fashion that seems consistent with microcrack link-up ahead of a main crack. Hardness and Young's modulus/hardness ratio were also studied as a function of crack density parameter.

2. EXPERIMENTAL PROCEDURE

2.1 Specimens

The chemical compositions and dimensions of initial rectangular yttrium chromite bar specimens are listed in Table 1 and the mechanical properties are listed in Table 2. The dopants were added to change yttrium chromite from an insulator to a semiconductor as part of a magnetohydrodynamic research project. Samples were fabricated by Trans-Tek Inc., Adamston, MD, from intimately mixed powders of chromium and yttrium [23]. The specimens were isostatically pressed at 207 MPa (30,000 psi) [24] and sintered at 1750 °C in flowing forming gas (a 95% nitrogen and 5% hydrogen mixture) in an electric furnace [19]. The average particle diameter for the starting powder was 1.3 microns as determined by sedimentation methods [23]. Details of powder mixing and calcining processes are given elsewhere [24]. The average grain size of sintered materials was approximately 6.0 microns, as determined from the linear intercept technique on scanning electron micrographs of fracture surfaces [25,26]. The density of green compacts was approximately 57% of the theoretical density. X-ray diffraction analysis confirmed that the specimens were orthorhombic (distorted perovskite structure) at room temperature.

2.2 Elasticity Measurements

Elasticity measurements were performed by the sonic resonance technique at room temperature in air. This technique was originated by

Table 1. The chemical compositions and dimensions of initial yttrium chromite specimens.

Specimens	Component	Mass (gm)	Length (Cm)	Width (Cm)	Thickness (Cm)	Mass Density (cm/gm^3)
YP10	$YCrO_3$	3.303	5.849	0.830	0.131	5.19
YP11	$YCrO_3$	3.447	5.849	0.830	0.135	5.16
Y0	$YCa_{0.05}CrO_3$	3.987	4.477	1.298	0.123	5.58
Y4	$YCa_{0.02}CrO_3$	2.505	5.122	0.672	0.128	5.69

Table 2. Mechanical properties of initial yttrium chromite specimens.

Specimen	Young's modulus (GPa)	Shear modulus (GPa)	Poisson's ratio	Bulk modulus (GPa)
YP10	66.9	29.2	0.146	31.5
YP11	61.2	27.3	0.122	26.9
Y0	245.5	98.5	0.246	161.4
Y4	260.5	105.9	0.236	160.8

Forster [27]. The experimental technique has been discussed in detail by Spinner and Tefft [28]. A schematic of the experimental apparatus is shown in Figure 1. A 2325A Synthesizer/Function Generator* was used to generate a known sinusoidal electric signal which was converted into a mechanical vibration of the same frequency by a high power model 62-1 piezoelectric driver transducer**. This mechanical vibration was transmitted to a suspended specimen through cotton thread and conveyed to the pick-up transducer through another suspension cotton thread at the other end of the specimen. The mechanical vibration was reconverted to an electrical signal which was amplified, filtered by 4302 Dual 240B/Octave Filter Amplifier***, and passed into an 8050A Digital Multimeter#. The digital voltmeter aided in detecting the resonant condition by giving a value of the amplitude at the pick up. A V-1100A Oscilloscope## gave a visual indication of the amplitude on the screen, so that the resonant frequency (maximum amplitude) could be estimated. Precise determination of the resonant condition was made using the digital voltmeter. The method of suspending specimens is shown in Figure 2 [28].

Nodal points are the positions of zero displacement in the vibration direction for each vibration mode. Nodal points were determined to obtain the fundamental flexural and torsional resonant frequencies. The fundamental flexural vibration has two nodal points,

*Hewlett Packard, Palo Alto, CA.

**Astatic Corporation, Conneaut, Ohio

***Ithaco, Ithca, NY.

#Fluke, Everett, WA.

##Hitachi, Tarrytown, NY

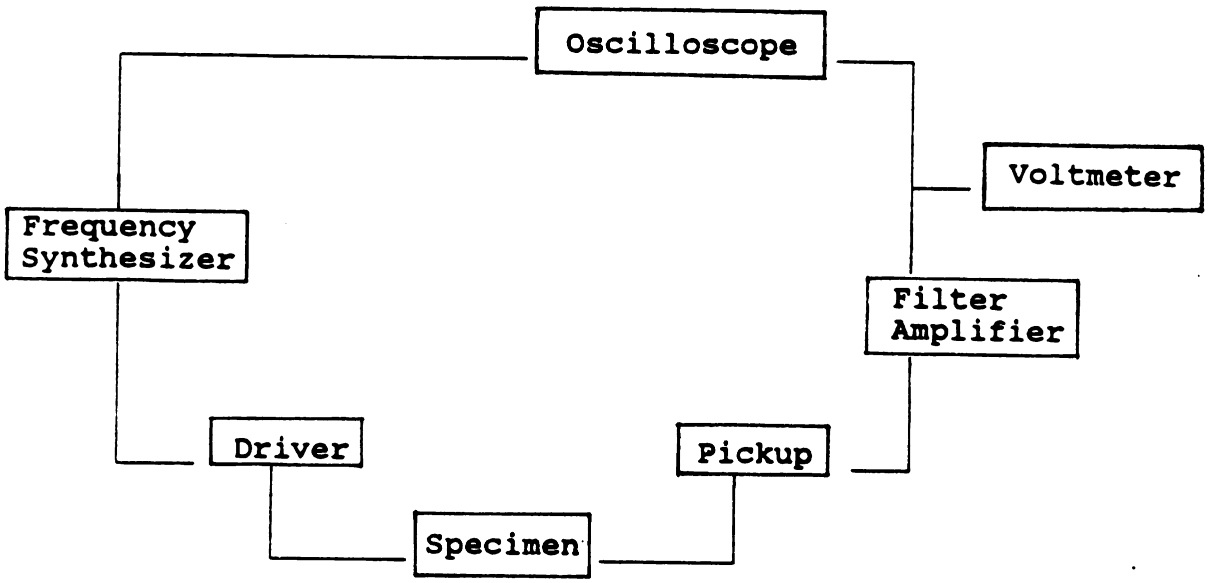

Figure 1. Schematic of the experimental appatatus of sonic resonance technique

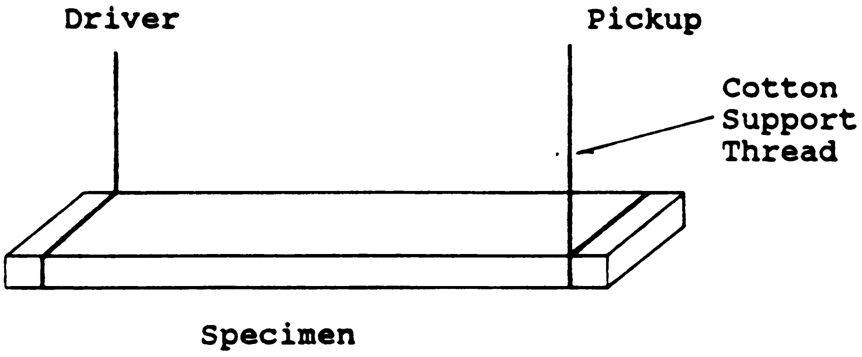

Figure 2. Specimen suspension method for the sonic resonance technique

one located at 0.224 L and the other node located at 0.776 L where L is the specimen length. The fundamental torsional vibration has one node point at the center. When a high signal amplitude was obtained at a frequency, a needle was put perpendicular to the length of the bar specimen keeping the frequency. Then, the amplitude was recorded as the position of the needle. When the amplitude at a frequency without a needle was the same to the amplitude at the frequency with a needle at a position, the position is the node point. The node points were determined at the frequencies of each high amplitude in this way. If the node points at a frequency with high amplitude are the same as the node points of the fundamental flexural vibration, the frequency is the fundamental flexural resonant frequency. Similarly, the fundamental torsional resonant frequency was obtained. There may be a slight shift of frequency when the thread is far from the position of node. So, the thread was positioned close to the nodes to obtain accurate results. Elasticity measurements were made by varying the oscillator frequency until the suspended specimen vibrated in a mechanical resonance vibration. At the resonance condition, the amplitude of vibration reached a maximum which was measured by the voltmeter and observed by the osilloscope [29]. The flexural and torsional resonance frequencies of each specimen were determined via the following equations.

Young's modulus, shear modulus and Poisson's ratio were caculated from the flexural and torsional frequency using the mass and dimension of specimen [28,30]. Equation (1) relates Young's modulus and flexural frequency for prisms of retangular cross section [30].

$$E = 0.94642dl^4f^2T/t^2 \qquad (1)$$

where E = Young's modulus

d = the mass density of specimen

l = the length of specimen

f = flexural resonant frequency

t = cross-sectional dimension in the direction of plane of vibration

T = correction factor for the prisms of rectangular cross section

The correction factor T in equation (1) is in turn given by

$$T = 1 + 6.585\,(1 + 0.0752\nu + 0.819\nu^2)\,(t/l)^2 - 0.868\,(t/l)^4 - \frac{8.340\,(1 + 0.2023\nu + 2.173\nu^2)\,(t/l)^4}{1 + 6.338\,(1 + 0.1408\nu + 1.53\nu^2)\,(t/l)^2} \qquad (2)$$

where ν = Poisson's ratio.

Equation (3) relates shear modulus to the torsional resonant frequency of the specimen.

$$G = d\,(2lf/n)^2 R \qquad (3)$$

where G = shear modulus

l = the length of specimen

f = torsional resonance frequency

n = the order of the vibrational mode, which is unity

for the fundamental mode, two for the first overtone, etc.

R = a shape factor which is a function of the shape of the cross section of the specimen.

For the prisms of rectangular cross-section, the shape factor R in equation (3) is given [28]

$$R = \frac{1 + (b/a)^2}{4 - 2.521(b/a)\ (1 - e^{v})} \left(1+ \frac{0.00851 n^2 b^2}{l^2} \right) - 0.060\ (\pi b/l)^{3/2}\ (b/a - 1)^2 \qquad (4)$$

where $v = \dfrac{1.991}{\Pi b/a}$

a and b = the cross-sectional dimensions of prismatic specimens, with restriction $b \geqq a$.

Poisson's ratio for a homogeneous isotropic body is caculated by

$$\nu = \frac{E}{2G} - 1 \qquad (5)$$

Using equation (5), one can calculate Poisson's ratio from experimentally determined values of shear modulus and Young's modulus.

2.3 Fracture Toughness Measurements

Fracture toughness was determined from Vickers indentation technique. Specimens were adhered to a 6.2 x 3.1 x 1.1 cm aluminium plate with Super Glue (Super Glue Corp., Holn, NY) in order to make it easier to hold the small specimens during the polishing process. Specimens were polished using 240, 320, 400 to 600 grit silicon carbide polishing papers (Mager Scientific Inc., Dexter, MI). Polishing was continued using rotating polishing machines with 5, 0.3 and 0.05 micron aluminium oxide powders (Mager Scientific Inc., Dexter, MI). Table 3 shows the typical time for each grit employed during the polishing procedure for each specimen. Total polishing time for an individual specimen was about about 5 hours. Polished specimens had very small flaws or pores as observed at 800 magnification by the Neophot 21 Optical Microscope (Leco, Warreendale, PA). An optical micrograph of the surface of a polished specimen is shown in Figure 3.

After polishing, specimens were removed from the aluminium plates by heating the specimens and aluminium plate in the wire-wound resistance furnace (type 59344 Lindberg) at 350^{0}C in air for 1 hour. This heat treatment caused the glue to decompose to the point where the specimens could be easily removed.

Elastic moduli were obtained for the polished specimens using the sonic resonance technique. Elastic moduli were compared with those of the polished specimens which were heated to remove the aluminum plate at 350^{0}C for 1 hour (see Result and Discussion).

The specimens were again glued to an aluminium plate with the super glue in order to perform the Vickers indentation test. The Vickers indentation test employs a pyramid-shaped diamond, which in turn produces a pyramidal-shaped indentation impression in the specimen. Radial cracks typically extend from the corners of the intent impression and propagate across the surface of the specimen (see Figure 4). The impression size and crack size relate to the hardness and the

Table 3. Polishing procedure used for each yttrium chromite specimen

Specimen	Silicon carbide polishing paper (grit)				Alumina polishing powder (microns)			
	240	320	400	600	600 grit	5	0.3	0.05
	(minutes)				(minutes)			
YP10	x	x	10	10	20	30	80	100
YP11	x	x	10	10	20	30	80	100
Y0	10	20	20	20	30	50	60	80
Y4	10	20	20	20	30	50	60	80

x means that polishing was not done at this condition

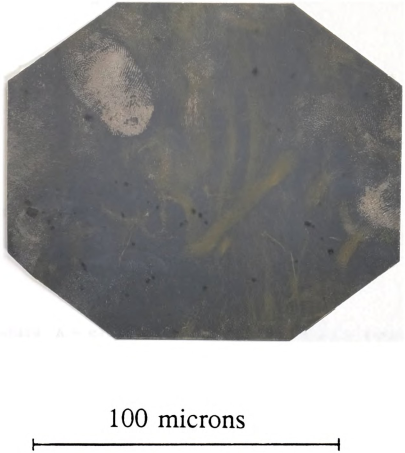

Figure 3. Optical micrograph of surface of polished specimen

fracture toughness of the indented specimen and to the applied load. Figure 4 gives a schematic of the indentation impression and the associated radial cracks. The hardness is computed from [31,32]

$$H = 0.47P / a^2 \tag{6}$$

where H = hardness

P = peak indentation load

2a = the length of the diagonal of the indent impression

The fracture toughness is given by [33,34]

$$K_c = A \, (E / H)^{1/2} (P / c^{3/2}) \tag{7}$$

where A = materials independent calibration constant and 0.016 ± 0.0004 for Vickers indentation [32]

E = the Young's modulus of the material

H = the hardness of the material

P = the peak indentation load

2c = the post-indentation crack length

The Vickers indentation test was done for yttrium chromite specimens using the Ser. No. DV-5987 semi-macro indentor of Buehler LTD, Lake Bluff, IL. Crack length and impression size were measured from the same apparatus. The crack length after Vickers indentation test should be immediately measured for the valid value of fracture toughness [32] because the crack length can change as a function of time after the test

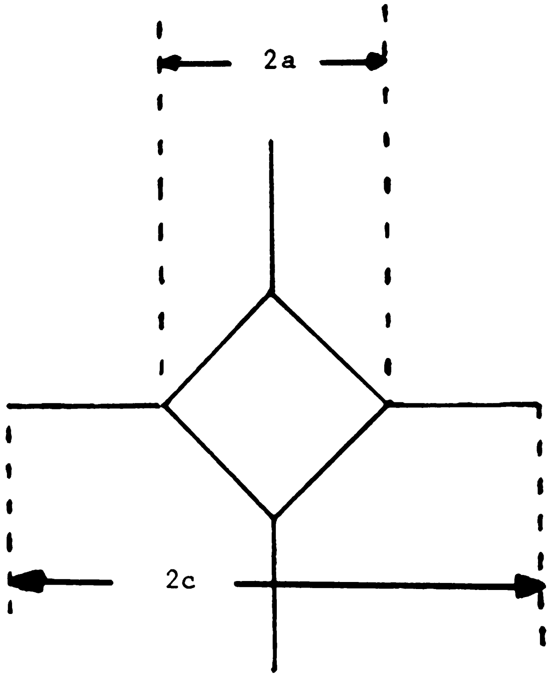

Figure 4. Indentation impression and radial crack geometry for Vickers indentation

owing to "the slow crack growth and crack-microstructure interaction." The crack length and impression size after the indentation test were measured within 20 and 40 seconds, respectively. The change of the crack length after the indentation test was so small that it was difficult to measure using the Ser. No. DV-5987 semi-macro indentor of Buehler LTD, Lake Bluff, IL.

2.4 Thermal Annealing

Thermal annealing changed the microcrack damage state of the specimens. The annealing times and temperatures are listed in Table 4. The mirocracked yttrium chromite specimens were healed by thermal anneals below the temperature of yttrium chromite phase transition temperature (1100 ^{0}C). The thermal anneals were performed in a wire wound resistance furnace of Lindberg type 59344 which had a maximum temperature capability of 1200 ^{0}C. The inside dimension of furnace was 40 x 20 x 15 cm.

The furnace used for heat treatment was lined with refractory bricks, so that precautions must be taken to assure that the specimen is not contaminated during the heating process by either the floor of the furnace or by "dusting" of the refractory brick onto the specimen. The surface of refractory bricks can degrade during heating, by mechanical and/or chemical processes. If the particles of "dust" freed by the degradation falls onto the specimen, the specimen can be contaminated during the annealing process. To minimize such contamination, the following protection was provided for the specimen. The specimens were annealed on a 5.2 x 1.0 x 0.1 cm alumina setter. The setter was placed on a refratory brick of 22.5 x 11.3 x 6.2 cm dimension. The specimens

Table 4. Annealing temperarures and times used in order to heal microcracks in yttrium chromite specimens

Specimen	Specimen before annealing	Temperature (^{o}C)	Time (hours)
YP10	YP10	x	x
YP21	YP10	1000	12
		1000	18
YP22	YP11	1000	18
		1020	18
YP23	YP21	1035	50
		1070	20
YP24	YP22	1035	20
		1095	20
Y0	Y0	x	x
Y4	Y4	x	x

x means that thermal annealing was not done at this condition.

were covered with an alumina boat of 4.8 x 1.1 x 0.9 cm dimension. The specimens, inside the alumina boats, were positioned 5 cm away from the thermocouple.

The furnace temperature was slowly increased and decreased, step by step, to prevent thermal shock damage. Heat treatment was done according to the following schedule: 30 minutes at 300°C, 30 minutes at 500°C, 30 minutes at 700°C, 30 minutes at 900°C, and at the assigned temperature and for the assigned time in Table 4. Cooling was done according to the following schedule: 40 minutes at 900°C, 1 hour at 700°C, 2 hours at 500°C. The furnace power was then turned off, and the furnace was allowed to cool for at least 3 hours before the door of the furnace was opened. The temperature of the furnace was about 170°C when the door was opened.

3. THEORETICAL REVIEW

3.1 Theories Relating Decrements in Young's Modulus to the Microcrack Density Parameter

The microcrack damage state of a polycrystalline is related to changes in the elastic moduli that accompany microcracking [21,35-38]. The studies of Walsh [35], Salganik [36], Budiansky and O'Connel [37], Hasselman and Singh [38], and Kemeny and Cook [39] proposed that the elastic moduli of a microcrocracked body is a function of ϵ, the crack density parameter.

$$\epsilon = N \langle a\rangle^{3} \tag{8}$$

where ϵ = crack number density parameter
N = microcrack number
$\langle a\rangle$ = mean microcrack radius

These theories each predict a similar microcrack density-modulus decrement behavior [21]. These theories [35-39] assumed a homogenous isotropic body with a number density N of randomly oriented cracks of mean radius $\langle a\rangle$. Walsh treated the case of elliptical cracks, Salganik treated the disk shaped cracks, Budiansky and O'Connel treated rectangular and circular cracks.

Kemeny and Cook assumed that a linear elastic, isotropic, homogeneous material contains a random distribution of flat, open cracks or external cracks where "external cracks" are identical to surface

breaking cracks. Kemeny and Cook treated the flat, external crack in two dimensions, and penny-shaped crack and external cracks in three dimensions. The relation between the intrinsic Young's modulus and the effective Young's modulus was given for a solid containing microcracks, loaded under a uniaxial stress σ [40] (in an expression similar to that of Budiansky and O'Connel [37]).

$$-\frac{\sigma^2 V}{2Y_0} = -\frac{\sigma^2 V}{2Y} + \Delta\phi \tag{9}$$

where $\Delta\phi$ = the increase in strain energy due to the presence of the voids (cracks or external cracks in this case)

V = the volume of the body containing the cracks

Y_0 = intrinsic Young's modulus

Y = effective Young's modulus

Kemeny and Cook utilized an axisymetric extention of Irwin's relation [41] between the energy release rate to extend a crack and the crack tip stress intensity factors K_1, K_2 and K_3. For a penny-shaped crack in three dimensions, the strain energy and the stress intensity factors are related by

$$U_e = \frac{(1-\nu_0^2)}{Y}\int_0^c [K_1^2 + K_2^2 + \frac{K_3^2}{(1-\nu_0)}] 2\pi c dc \tag{10}$$

where U_e = the additional strain energy due to a single crack of length 2c in a three dimensional elastic body

ν_0 = the intrinsic Poission's ratio

K_1, K_2 and K_3 = the crack tip stress intensity for opening, shearing, and tearing modes of deformation, respectively

2c = the length of penny-shaped crack

The stress intensity factors taken from Rice [42] are given by

$$K_1 = \frac{2}{\pi} \sigma \sin^2\gamma(\pi c)^{1/2}$$
$$K_2 = \frac{4}{\pi(2-\nu_0)} \sigma \sin\gamma\cos\gamma\cos\omega(\pi c)^{1/2} \qquad c<<\omega \qquad (11)$$
$$K_3 = \frac{4(1-\nu_0)}{\pi(2-\nu_0)} \sigma \sin\gamma\cos\gamma\sin\omega(\pi c)^{1/2}$$

where σ = uniaxial stress

γ = the angle between the xy plane and the radius vector

ω = the azimuthal angle

Kemeny and Cook substituted the stress intensity factor taken from Rice into equation (10), and used the relations of $<\sin^2\omega> = <\cos^2\omega> = 1/2$, $<\sin^4\gamma> = 1/5$ and $<\sin^2\gamma\cos^2\gamma> = 2/15$. Assuming that there are N penny shaped cracks in the body with a mean crack radius cubed $<c>^3$, Kemeny and Cook gave

$$U_e = \frac{8}{45Y} N\sigma^2 <c>^3 (1-\nu_0^2) \frac{10 - 3\nu_0}{2 - \nu_0} \qquad (12)$$

where U_e = the total strain energy due to a random distribution of penny-shaped cracks

N = the number of penny-shaped cracks

$<c>^3$ = a mean crack radius cubed

In an appendix 1, equation (12) is derived using equation (10) and K_1, K_2 and K_3 values from equation (11).

Substituting equation (12) in equation (9), Kemeny and Cook gave the following relation

$$Y = Y_0 \; [\; 1-f(\nu_0)\epsilon \;] \tag{13}$$

where Y = the Young's modulus for a microcracked material

Y_0 = the Young's modulus for a nonmicrocracked material

ν_0 = the Poisson ratio for a nonmicrocracked material

ϵ = crack density parameter

The function $f(\nu_0)$ is given by [36]

$$f(\nu_0) = \frac{16(10-3\nu_0)(1-\nu_0)}{45(2-\nu_0)} \tag{14}$$

From equations(8) and (13)

$$\Delta Y = \frac{Y_0 - Y}{Y_0} = f(\nu_0)N <a>^3 \tag{15}$$

That is

$$\epsilon = N<a>^3 = \frac{\dfrac{Y_0-Y}{Y_0}}{f(\nu_0)} = \frac{\Delta Y}{f(\nu_0)} \tag{16}$$

From equation (16), the microcrack damage state of a specimen can be determined from the change of Young's modulus that is induced by thermal annealing. Solving for ϵ uses the experimentally determined values of Y, Y_0 and ν_0.

The experimental determination of the quantities N and $<a>^3$ is difficult. For example, when a specimen is observed in a microscope, the microcrack state of the specimen surface can be different from that of specimen bulk. The differences in the microcrack state can result from surface damage by the manufacturing process. Also, the stress state of a specimen surface is different from that of bulk. It is very difficult to experimentally determine both the inherent microcrack number N and inherent microcrack size <a>. However, the microcrack density parameter can be determined directly from the decrement in modulus, as shown in equation (16).

3.2 The Formation of Microcracks

Microcracks can be formed in a number of ways, including thermal expansion mismatch and phase transformation. One example of thermal expansion mismatch is thermal expansion anisotropy of a noncubic material. Noncubic materials have different thermal expansion coefficients along the crystalline axes. As a polycrystalline body cools from high temperature, thermal expansion anisotropy can lead to localized stresses that in turn induce stored elastic strain energy. This stress can result in internal microcracking in brittle materials [11,13,43]. Microcracking due to thermal expansion anisotropy can be very pronounced for specimens with grain sizes larger than a critical grain size, while specimens with a grain size smaller than the critical grain size do not microcrack [11-13, 43].

Thermal expansion mismatch also can occur in multi-phase materials [12]. The stress owing to the difference of thermal expansion coefficients between phases causes microcracks. Microcracking in multiphase materials is a function of the thermal expansion coefficient, volume fraction, particle size, and elastic properties of each phase [12]. Microcracks from the thermal expantion mismatch typically form at the grain boundaries [44].

Microcracks also can result from the localized internal stresses due to rapid volume changes of grains from phase transformation. Twins are frequently formed by phase transformation in ceramics. Such twins can reduce the macroscopic shape change of the transforming particle or grain. Shear strains form at the twinned regions [45], so the large stress concentrations can occur at twin interfaces and stress results in microcrack nucleation.

The interaction of a moving crack with pre-existing microcracks can be considered in terms of the following two cases.

(1). Microcracks may link-up ahead of a moving crack. Then, fracture toughness may decrease as a function of increasing the microcrack number density (Figures 5 and 6) by decreasing the fracture surface area formed by the moving crack. Microcrack link-up may occur if a) the microcracks are highly oriented, so that the vectors drawn normal to the microcrack planes point in a single direction, or b) the plane of the moving crack is coincident with microcracks.

(2). Microcracks ahead of the moving crack may produce multiple crack branching. In this case, fracture toughness may increase with increasing microcrack number density (see Figure 5 and 7) due to the contribution of small, branching cracks splitting off the moving

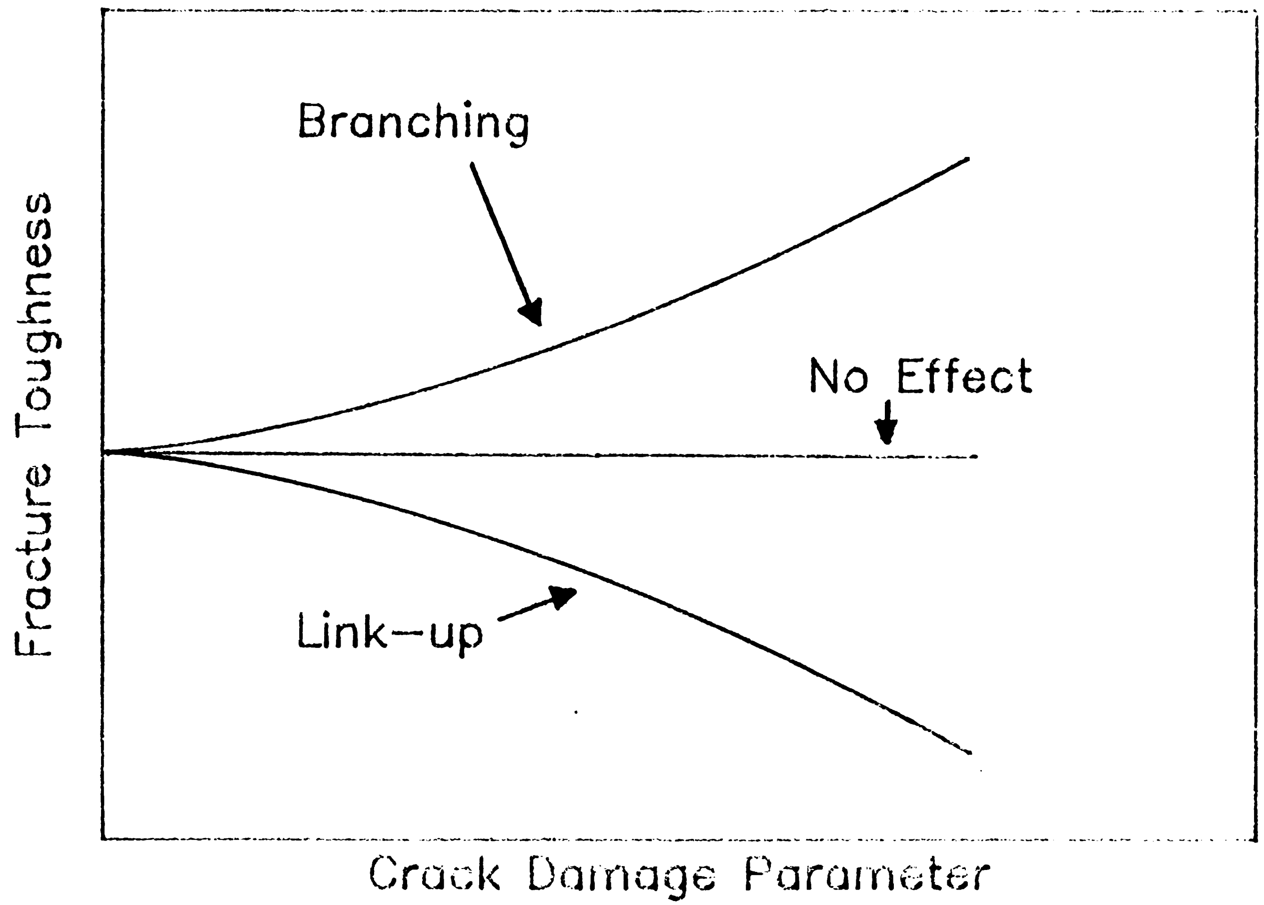

Figure 5. Fracture toughness versus crack density parameter according to microcrack link-up and branching models

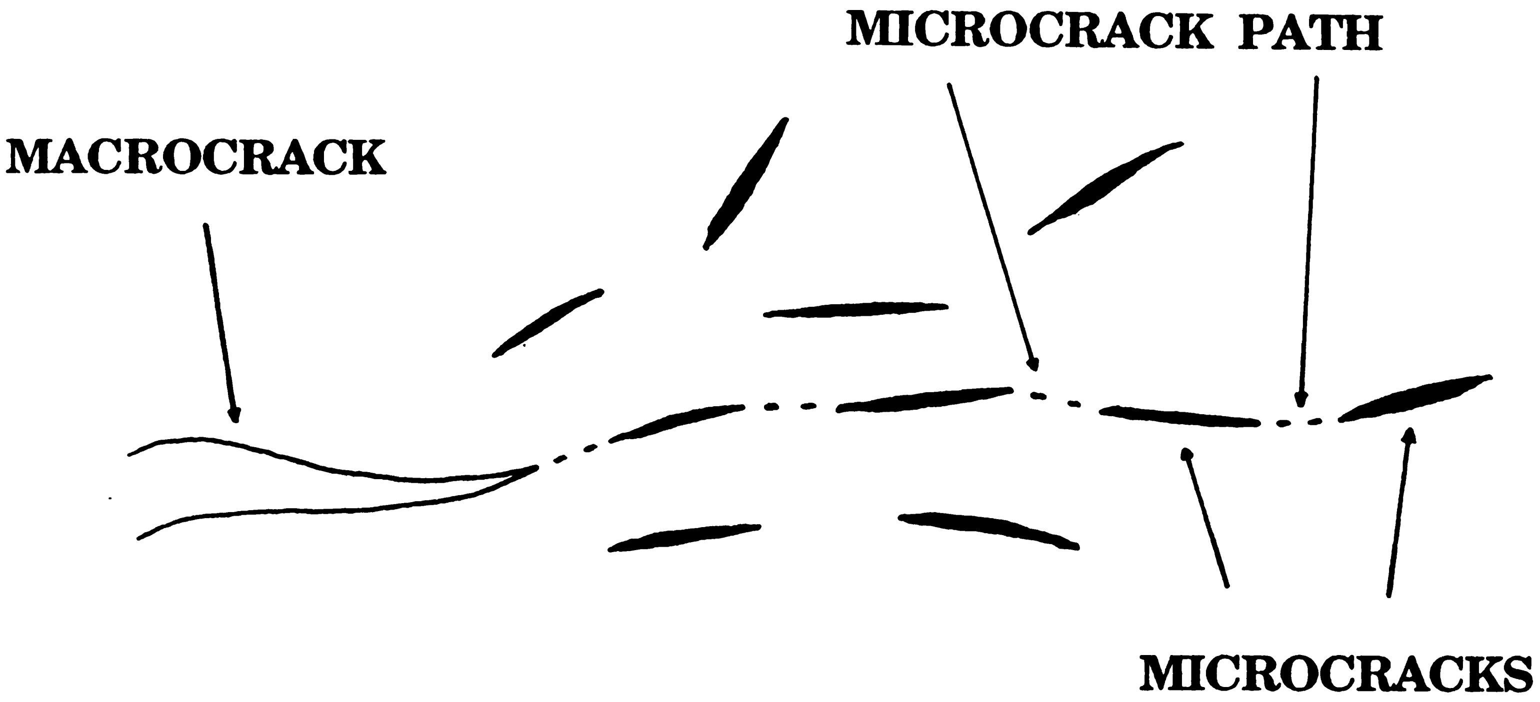

Figure 6. Schematic of the possible macrocrack-microcrack interaction that could lead to microcrack link-up

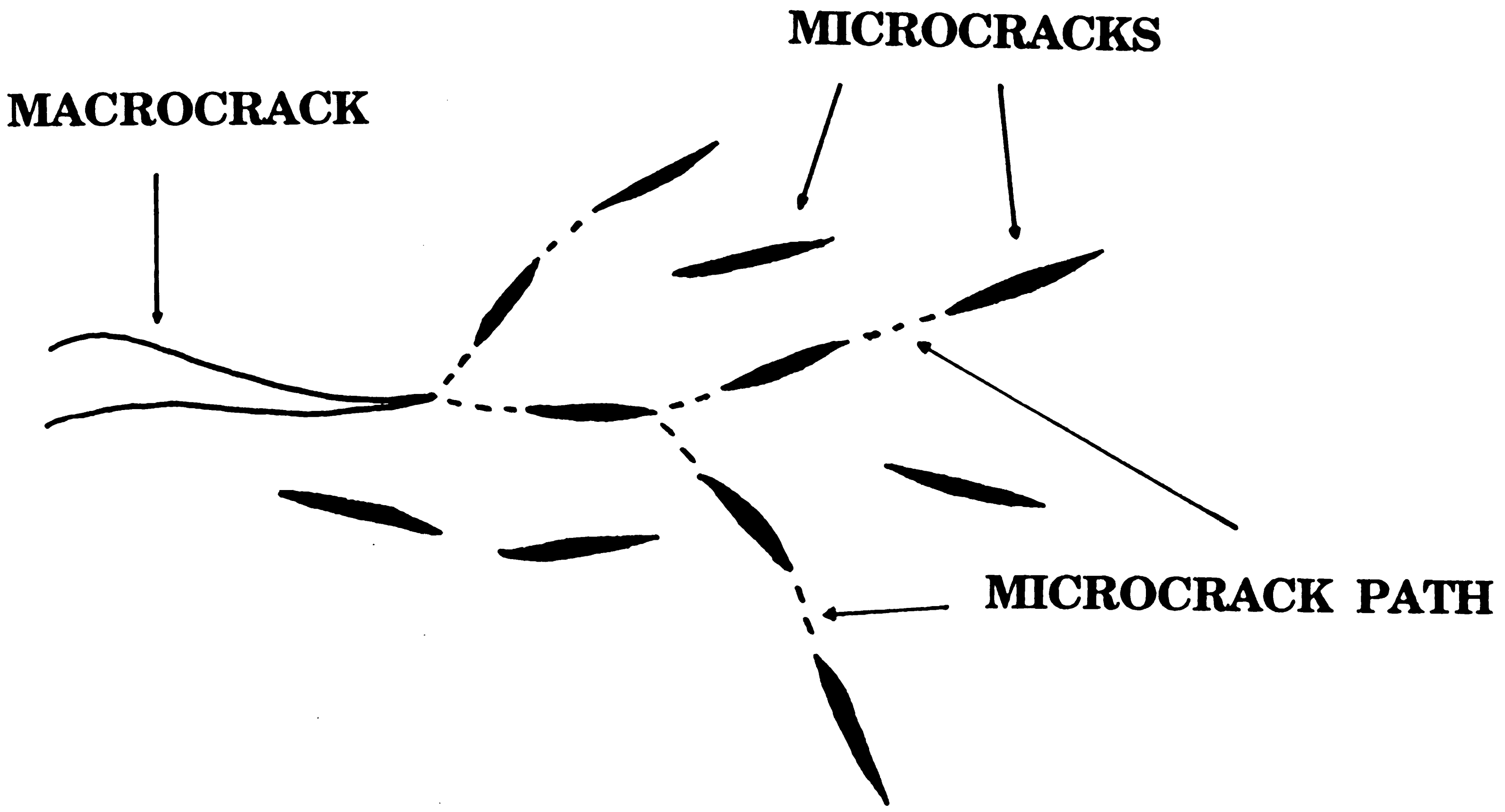

Figure 7. Schematic of the possible macrocrack-microcrack interaction that could lead to microcrack branching

microcrack. This might occur if the preexisting microcracks are oriented favorably for crack branching.

3.3 Studies of Fracture Toughness of Microcracked Materials

Rose considered a two dimensional configuration which has a semi-infinite main crack with a collinear microcrack (see Figure 8) [46]. For this configuration, Rose derived formulas for the stress intensity factor at a main crack tip and two tips of a microcrack, and estimated the fracture toughness degradation by microcracks linking up ahead of a main crack. Rose assumed that the main crack was a semi-infinite crack in an infinite body and, "the nominal stress field is given by the singular term in the near-tip asymtotic expansion for an elastic crack-tip stress field; the component of the nominal stress tensor is given relative to the polar coordinates(r,θ) with the main crack tip as origin."

$$\sigma_{\alpha\beta}(r,\theta) = [\ K^n/(2\pi r)^{1/2}\ ]\ f_{\alpha\beta}(\theta) \tag{17}$$

where K^n = the nominal (mode 1) stress intensity factor

Rose considered that, "the problem is to determine the resulting stress field", for the configuration in Figure 8. Rose obtained the boundary conditions for the model in Figure 8 as follows.

$$\sigma_{yy} = \sigma_{xy} = 0 \tag{18}$$

for $y \to \pm 0$ along $-\infty < x < 0$, and $a < x < b$;

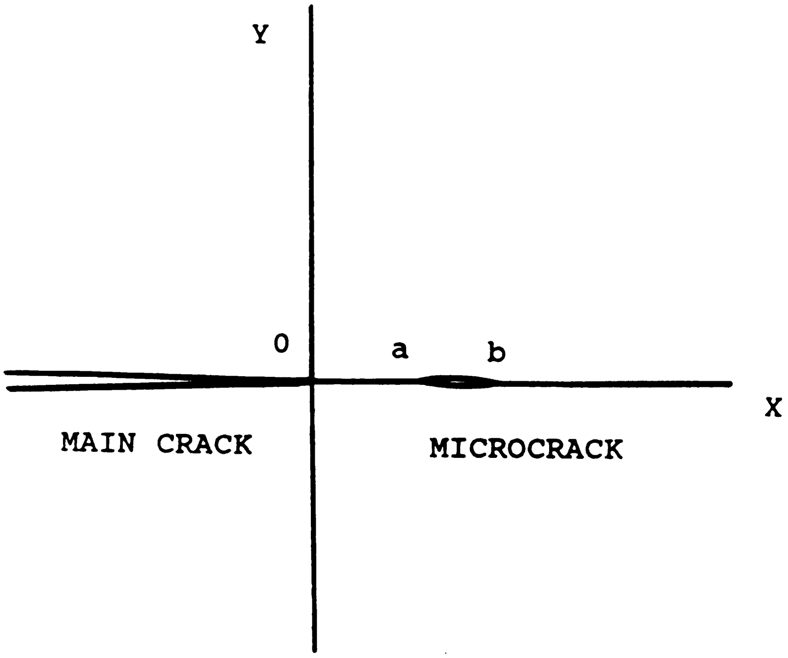

Figure 8. Semi-infinite main crack collinear with two dimensional microcrack

$$\sigma_{\alpha\beta}(r,\theta) \rightarrow \sigma_{\sigma\beta}{}^{n}(r,\theta) \qquad \text{for } r>>b \tag{19}$$

Rose solved the problem using a conformal trasformation ($z \rightarrow \zeta = \sqrt{z}$) and obtained, "the transformed boundary conditions in the ζ-plane corresponding to those for two collinear cracks of equal length perturbing a uniform stress field." Reverting the known solution to the z-plane, Rose obtained

$$Z(z) = K^{n}(z - bC)/[2\Pi z(z-a)(z-b)]^{1/2} \tag{20}$$

$$C = E(k')/K(k') \tag{21}$$

$$k^{2} = a/b \qquad k' = (1 - a/b)^{1/2} = (1 - k^{2})^{1/2} \tag{22}$$

where K and E = the complete elliptic integrals of the first and second kind, respectively

k and k' = the modulus and complementary modulus, respectively, for the elliptic integrals

Rose obtained the stress intensity factor at the three crack tips from equation (18) as follows.

$$K(x=0)/K^{n} = C/k \tag{23}$$

$$K(x=a)/K^{n} = (C-k^{2})/kk' \tag{24}$$

$$K(x=b)/K^{n} = (1-C)k' \tag{25}$$

where K^{n} = the nominal (mode 1) stress intensity factor

Considering an isotropic elastic material permeated by a homogeneous and isotropic distribution of microcracks, Rose obtained

$$L = N^{-1/3} \tag{26}$$

where N = the average number of microcracks per unit volume

L = the average distance between neighboring microcracks

Rose supposed that, "a planer main crack of characteristic linear dimension much larger than L is introduced into microcracked material, is made to grow quasi-statically, and the pre-existing microcracks do not grow themselves during the main-crack growth but link up with the main crack if they lie on, or close to, the fracture plane." Then,

$$A = N^{2/3}\langle c^2\rangle \tag{27}$$

$$a/b = \frac{b - (b - a)}{b} = 1 - A \tag{28}$$

where A = the area fraction of the fracture plane corresponding to pre-existing microcracks

$\langle c^2\rangle$ = the average of the projected area of the microcracks onto the fracture plane.

Regarding, "the linking up of the main crack with this collinear microcrack as an idealized repeat unit in the crack growth process and the effect of all the other microcracks being accounted for by a uniform reduction in the effective modulus" [46], Rose derived an estimate for K_0, the effective fracture toughness of a microcracked body, from equation (23)-(25). Then, if one compares the magnitude of the stress intensity factor, K, at the three crack tip positions (x=0, x=a, x=b) in Rose's model, the relative magnitudes of the K's are: K(x=0) > K(x=a) >

$K(x=b)$ of three crack tips. If it is assumed that, "crack extention occur at either of these crack tips when the relevent K reaches a definite critical value K_c, then, under increasing K^n, crack extention would begin from the main crack tip, and if K^n is kept constant, the link-up of the main crack with the microcrack would proceed unstably, rather than quasi-statically." If K_0 is the K^n at which link-up occurs, Rose derived.

$$K_0/K_c = k/C \tag{29}$$

where K_0 = an estimate of the effective fracture toughness of a microcracked body

K_c = the intrinsic fracture toughness of the material without microcracks.

Rose compared equation (29) with the estimate based on a rule of mixtures for the work of fracture [2,47], which gave

$$K_0/K_c = (1 - A)^{1/2} = (a/b)^{1/2} = k \tag{30}$$

From the estimate based on a rule of mixtures for K [10,48], Rose gave

$$K_0/K_c = 1 - A = a/b = k^2 \tag{31}$$

4. RESULT AND DISCUSSION

4.1 Experimental Result

Table 5 lists the Young's modulus, Y, Shear modulus, G, and Poisson's ratio, ν, obtained from the sonic resonance method for microcracked specimens. Table 5 shows that Young's modulus, shear modulus and Poisson's ratio typically decrease with increasing the crack density parameter (i.e. decreasing Young's modulus, Y). These elastic moduli in Table 5 were values for the polished specimens which were adhered to mounting aluminium plates and after polishing, the plate and specimen were heated at 350 ^{0}C for 1 hour to remove the plate. Young's modulus, Shear modulus and Poisson's ratio are compared with the values of the unpolished specimens in Table 6. Polishing and the heat treatment to remove the polishing plate did not greatly affect the elastic moduli of yttrium chromite specimens (Table 6).

The Young's modulus, Y_0 and Poisson ratio, ν_0 of nonmicrocracked, theoretically dense, yttrium chromite polycrystal were 280 GPa and 0.28, respectively [21].

From the measured Young's modulus, Y, for microcracked yttrium chromite specimens, and the Young's modulus and Poisson's ratio for nonmicrocracked yttrium chromite, the crack density parameter of each specimen was determined using equations (14) and (16). The crack density parameters of non-reheated specimens YP10, Y0 and Y4 were 0.436, 0.071 and 0.040, respectively. The crack density parameters of reheated specimens YP21, YP22, YP23 and YP24 were 0.355, 0.299, 0.272 and 0.209. The original specimens YP10 and YP11 were reheated and labeled as YP21,

Table 5. Crack density parameter and mechanical properties for the yttrium chromite specimens

Specimen	Crack density parameter	Young's modulus (GPa)	Shear modulus (GPa)	Poisson's ratio
YP10	0.436	66.9	29.2	0.146
YP21	0.355	106.9	45.1	0.181
YP22	0.299	133.8	54.9	0.219
YP23	0.272	147.0	61.2	0.202
YP24	0.209	178.0	71.9	0.239
Y0	0.071	245.5	98.5	0.246
Y4	0.040	260.5	105.9	0.236

Table 6. Comparison of elastic moduli of unpolished specimens with those of polished specimens which were adhered to the mounting aluminium plate and heated at 350^{0}C for 1 hour to remove the plate after polishing

Specimen	Y_{aft}/Y_{bef} (percent change in Y)	G_{aft}/G_{bef} (percent change in G)	ν_{aft}/ν_{bef} (percent change in ν)
YP22	133.8/137.2 (-2.5)	54.9/58.0 (-5.6)	0.219/0.183 (19.7)
YP23	147.0/145.1 (1.3)	61.2/59.7 (2.5)	0.202/0.215 (-6.0)
Y4	260.5/264 (-1.3)	105.9/106.4 (-0.5)	0.236/0.240 (-1.7)

Y_{bef}, G_{bef} and ν_{bef} mean the elastic moduli of specimens before polishing

Y_{aft}, G_{aft} and ν_{aft} mean the elastic moduli of specimens which were adhered to the mounting alumium plate, polished and heated at 350^{0}C for 1 hour to remove the plate

YP22, YP23 and YP24 according to each annealing condition. Table 4 in section 2.4 of this thesis lists the heat treatments and the associated specimen labels.

The crack density parameters calculated on the basis of elastic modulus change only do not include the effect of the specimen porosity. The measured Young's modulus is the function of both the microcrack density and the porosity. If we assume that the Young's modulus change due to the microcracks and porosity are independent, then,

$$Y_{meas} = Y_0 - Y_{micr} - Y_{por} \qquad (32)$$

where Y_{meas} = the measured Young's modulus

Y_0 = the Young's modulus of completely dense, non-microcracked yttrium chromite

Y_{micr} = the Young's modulus change due to microcracking

Y_{por} = the Young's modulus change due to porosity

The porosities of the non-reheated and the reheated specimens are listed in Table 7. Hence, Y_{por} for each specimens was determined from Mackenzie's equation as follows [47].

$$Y_{por} = Y_0 - Y_0\ (1 - 1.9p + 0.9p^2) = Y_0\ (1.9p - 0.9p^2) \qquad (33)$$

where Y_0 = the Young's modulus of material without porosity

p = the porosity

From equation (33), Y_{por} was determined for each specimen using a Y_0 of 280 GPa for the completely dense and non-microcracked yttrium chromite.

Table 7. The crack density parameter without porosity correction, ϵ_1, and the crack density parameter after porosity correction, ϵ_2.

Specimen	Young's modulus (GPa)	porosity (%)	ϵ_1	ϵ_2	% change
YP10	66.9	9.74	0.436	0.335	23
YP21	106.9	9.50	0.355	0.255	28
YP22	133.8	9.69	0.299	0.199	33
YP23	147.0	9.21	0.272	0.1762	35
YP24	178.0	9.22	0.209	0.113	46
Y0	245.5	3.05	0.071	0.037	48
Y4	260.5	0.99	0.040	0.029	10

If we consider the microcrack effect and porosity effect for the crack density parameter, then using equation (32), equation (15) can be rewritten as

$$\epsilon = \frac{\dfrac{Y_0 - (Y_0 - Y_{micr})}{Y_0}}{f(\nu_0)} = \frac{\dfrac{Y_0 - Y_{meas} - Y_{por}}{Y_0}}{f(\nu_0)} \tag{34}$$

From equation (34), the crack density parameter after porosity correction was calculated for each specimen. Table 7 lists the crack density parameter without porosity correction, ϵ_1, the crack density parameter with porosity correction, ϵ_2, and the percentage change due to the porosity correction.

Figure 9 shows the Young's modulus versus the crack density parameter with porosity correction. Young's modulus typically decreases linearly as a function of increasing density parameter. The deviation from linearity was perhaps due to the different porosity for each specimen.

Table 8 shows the values of hardness, H, fracture toughness, K_c, and Young's modulus/Hardness ratio (Y/H) at each load for each of the yttrium specimens. When specimens having low Young's modulus (YP10 and YP21) were indented at high indentation load (for example, 5.88 N or 9.8 N), a great deal of chipping and many cracks were observed around the impression, making it difficult to measure the impression sizes and crack sizes exactly. When these specimens were indented at the low indentation loads (for example, 0.98 N), cracks were not observed near the indent impression. This phenomena is referred to as the existence of a critical load, below which no cracking is observed [31-34]. Hence,

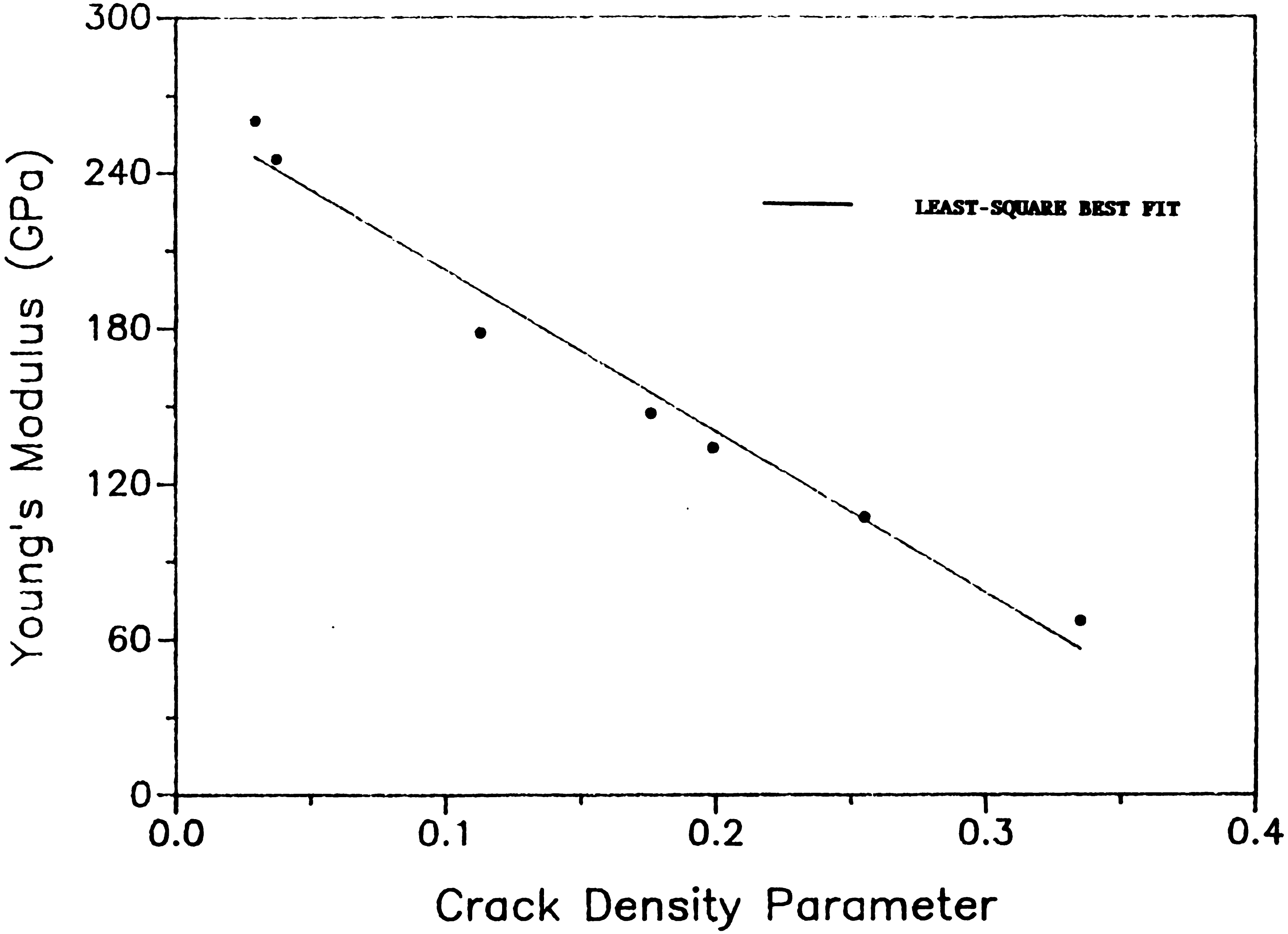

Figure 9. Young's modulus versus crack density parameter with porosity correction

Table 8. **Hardness, fracture toughness, and Young's modulus/hardness ratio for yttrium chromite specimens at each value of indentation load**

Specimen	Y (GPA)	Load (N)	<H> (GPa)	$<K_c>$ ($MPam^{1/2}$)	<Y/H>	Number of indentations
YP10	66.9	2.94	5.815	1.367	11.50	6
YP21	106.6	2.94	6.662	1.374	16.00	6
		4.9	6.950	1.562	15.34	6
YP22	133.8	2.94	8.173	1.277	16.37	6
		4.9	8.107	1.517	16.51	6
YP23	147.0	2.94	8.327	1.541	17.65	8
		4.9	8.584	1.449	17.12	8
YP24	178.0	2.94	9.260	1.601	19.22	6
		4.9	9.451	1.771	18.83	6

Table 8 (continued)

Y0	245.5	4.9	12.31	1.717	19.94	6
		9.8	13.04	1.828	18.83	6
Y4	260.5	4.9	13.04	1.757	19.98	6
		9.8	13.80	1.888	18.88	6

crack sizes were measured at 2.94 N for YP10 specimen, 2.94 N and 4.9 N for YP21, YP22, YP23 and YP24, and 4.9 N and 9.8 N for Y0 and Y4.

A plot of the hardness versus crack density parameter shows hardness decreasing in an approximately linear fashion with increasing crack density parameter (Figure 10 (a) and (b)). Thus, as the crack density parameter increases, microcracks formed upon cooling the specimen by the phase transformation in yttrium chromite at 1100^{0}C apparently reduce the measured hardness. The hardness versus crack density parameter data was fit to a linear equation of the form of equation (35), using the least-square best fit method.

$$H = A - B\epsilon \qquad (35)$$

where H = measured hardness (GPa)

ϵ = crack density parameter

A = 13.92 and 13.23 for the hardness versus crack density parameter without porosity correction and with porosity correction, respectively

B = 19.52 and 24.45 for the hardness versus crack density parameter without porosity correction and with porosity correction, respectively

Figure 11 (a) and (b) show the fracture toughness versus crack density parameter for microcracked yttrium chromite. Fracture toughness decreased with increasing crack density parameter. The fracture toughness versus crack density parameter data was fit to a linear equation using the least-square best fit

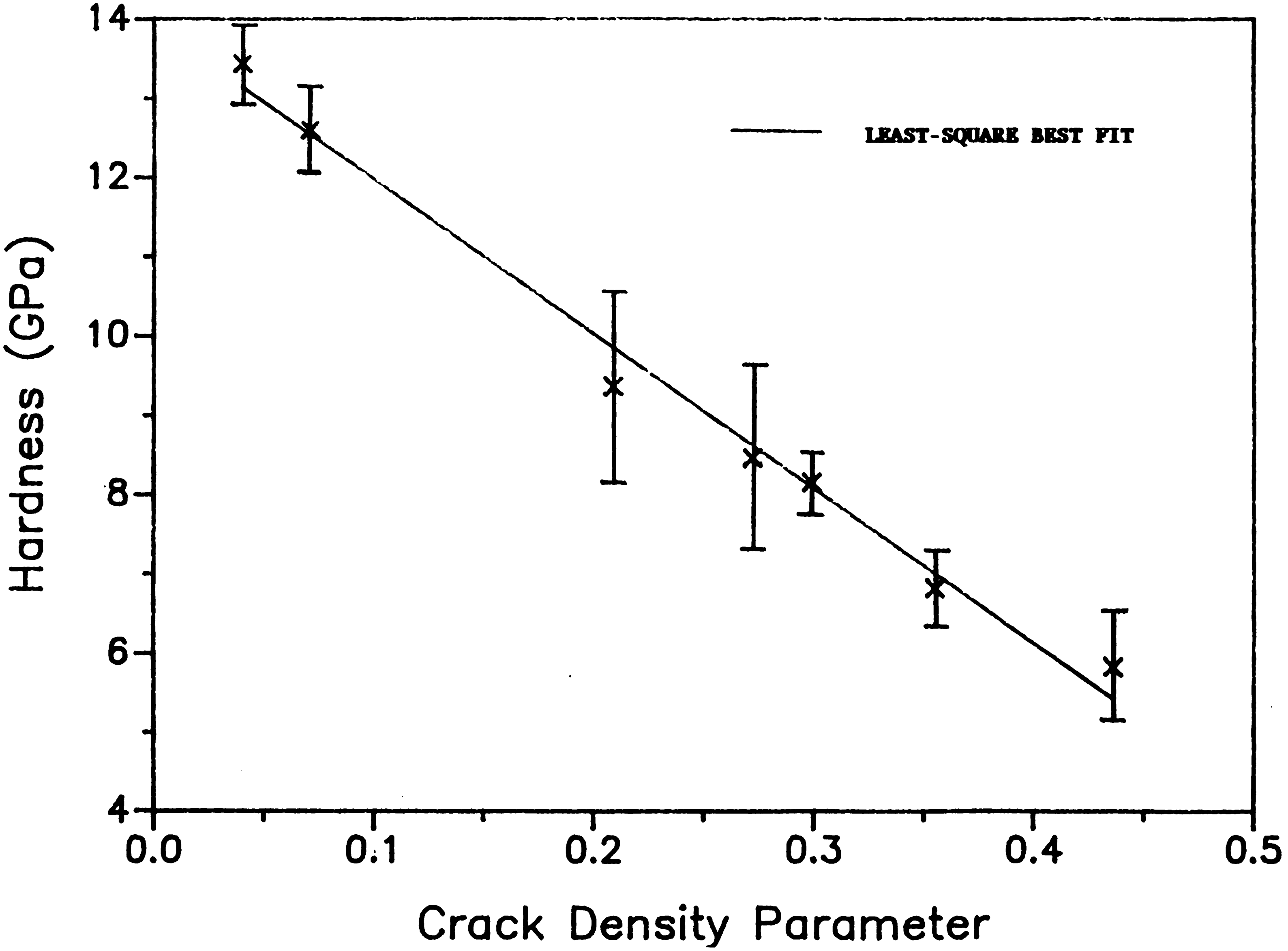

Figure 10 (a). Hardness versus crack density parameter without porosity correction for yttrium chromite. Error bars indicate ± S range where S = standard deviation.

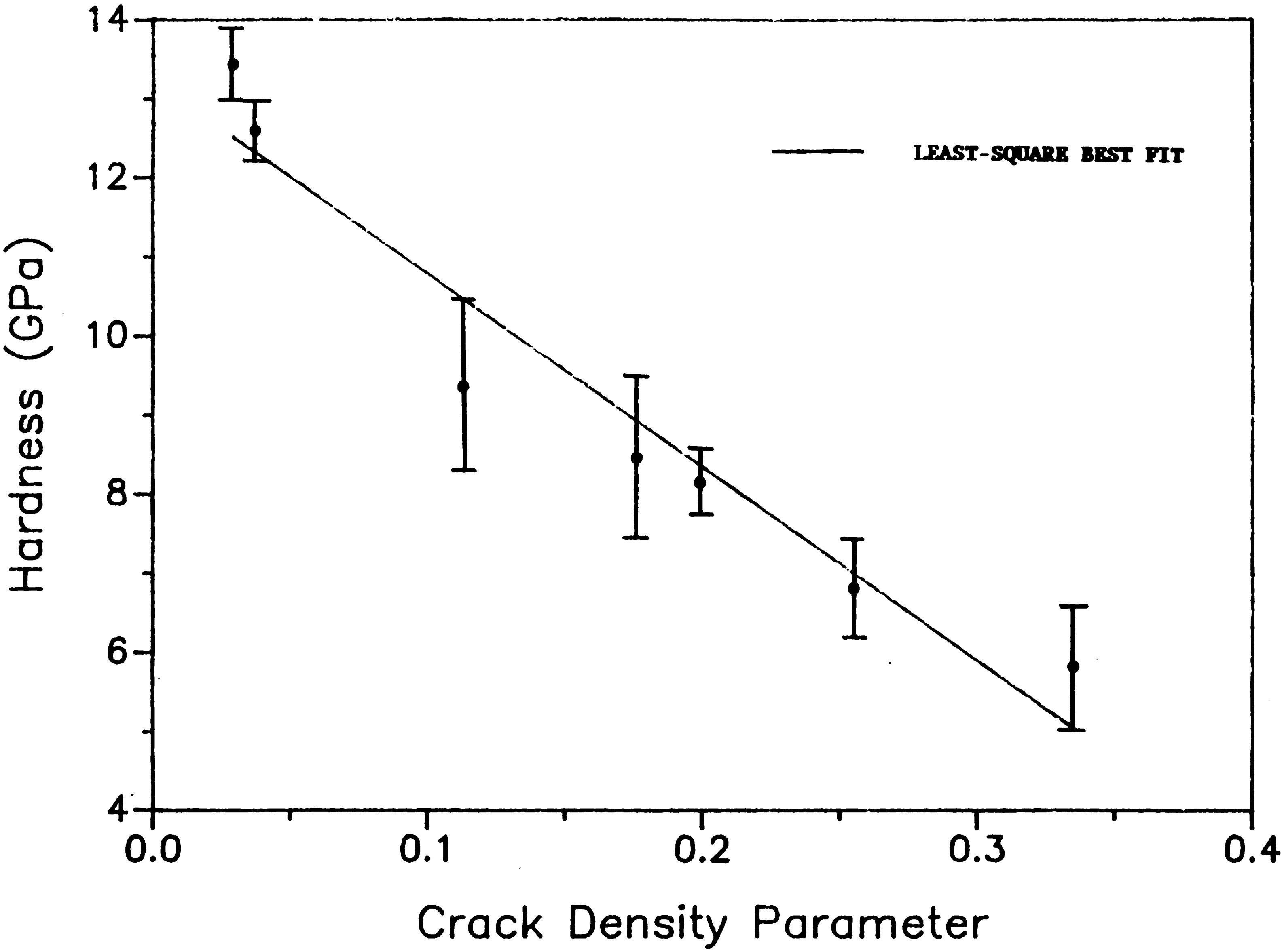

Figure 10 (b). Hardness versus crack density parameter with porosity correction for yttrium chromite. Error bars indicate ± S range where S = standard deviation.

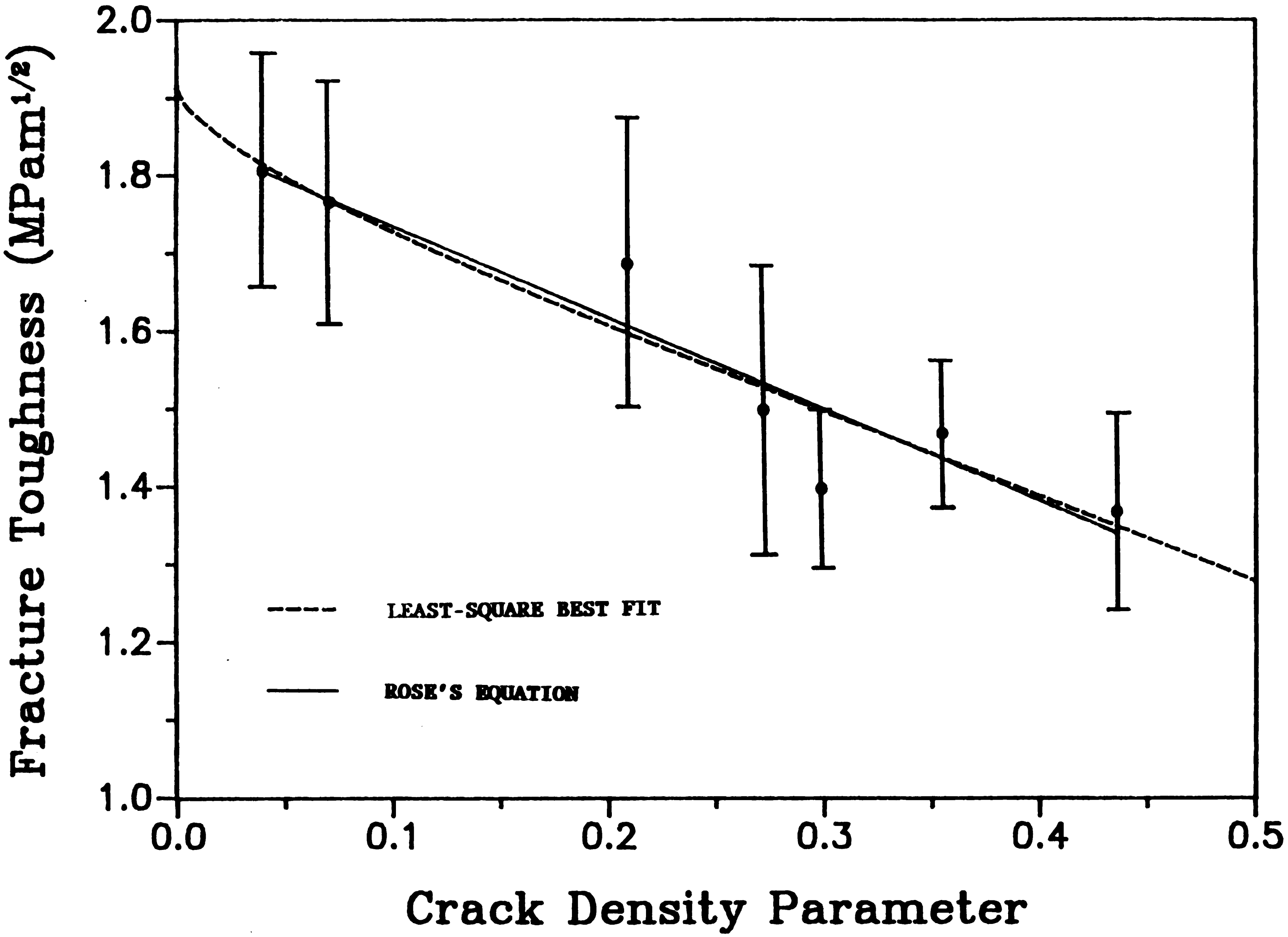

Figure 11 (a). Fracture toughness versus crack density parameter without porosity correction for yttrium chromite. Error bars indicate ± S range where S = standard deviation.

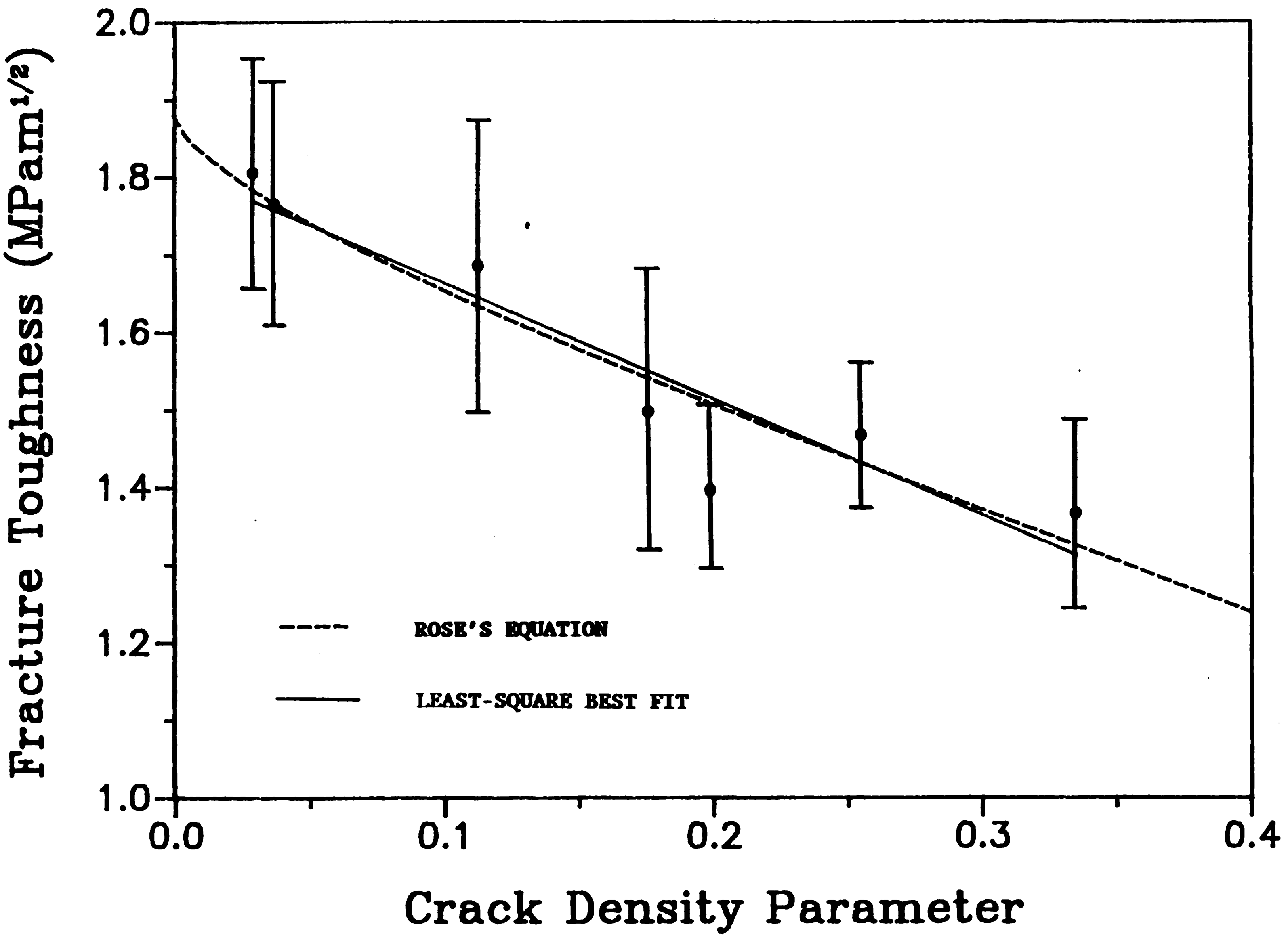

Figure 11 (b). Fracture toughness versus crack density parameter with porosity correction fot yttrium chromite. Error bars indicate ± S range where S - standard deviation.

$$K_c = C - D\epsilon \tag{36}$$

where K_c = Fracture toughness (MPam$^{1/2}$)

ϵ = crack density parameter

C = 1.853 and 1.815 for ϵ without porosity correction and with porosity correction, respectively

D = 1.177 and 1.498 for ϵ without porosity correction and with porosity correction, respectively

Equation (36) implies that pre-existing microcracks formed by high temperature phase trasformation of yttrium chromite decrease the fracture toughness and the microcrack link-up ahead of a moving macrocrack.

Young's modulus of the specimen is greater than 0 because $Y \leq 0$ means that specimen is falling apart. If we consider Young's modulus from equation (13),

$$Y = Y_0 \ (1 - f(\nu_0)\epsilon) > 0$$

$$\epsilon < \frac{1}{f(\nu_0)} \tag{37}$$

For this study, Y = 0 at $\epsilon = 0.573$, so physically meaningful values of ϵ must be less than 0.573. The expression for $f(\nu_0)$ is obtained from equations (14) and (16), where $\nu_0 = 0.28$. Similarly, if we consider hardness from equation (35), the hardness of specimen must be greater than 0. Thus, the crack density parameter must be less than 0.713 and 0.541 for ϵ without the porosity correction and with porosity correction. When we consider the fracture toughness from equation (36),

fracture toughness must be greater than 1.574 and 1.212 for ϵ without porosity correction and with porosity correction, respectively. If we compare to ϵ for Y = 0, H = 0 and $K_c = 0$, the crack density parameters for Y = 0 and H = 0 are similar. However, the crack density parameter for $K_c = 0$ is greater than those for Y = 0 and H = 0.

Figure 12 (a) and (b) show the ratio of Young's modulus/hardness versus crack density parameter for microcracked yttrium chromite. It is difficult to determine a mathmatical expression for this relation. The trend is that Young's modulus/hardness ratio is approximately constant as a function of the crack density parameter for the range of low crack density parameter. But, Young's modulus/hardness ratio decreases with increasing the crack density parameter for the range of high ϵ.

Figures 13 and 14 are optical micrographs of the indent impression and radial crack system for yttrium chromite specimens indented at 5.88 N and 9.8 N. For specimens having a low crack density parameter (that is, high Young's modulus) such as Y0 and Y4 specimens, a clear indent impression and crack form from the Vickers indentation test. This phenomenon is shown in Figures 13 and 14 for specimens Y0 and Y4 which have a low crack density parameter. However, for specimens having a high crack density parameter (that is, low Young's modulus) such as YP10 and YP21, considerable chipping and many small cracks formed around the indent impression at indentation loads higher than 4.94 N (see Figure 15). Cracks did not form at the surface of specimens for indentation loads less than 1.96 N. Thus, it was difficult to obtain the only crack emanated from the 4 corners of impression for specimen having a crack density parameter higher than 0.27.

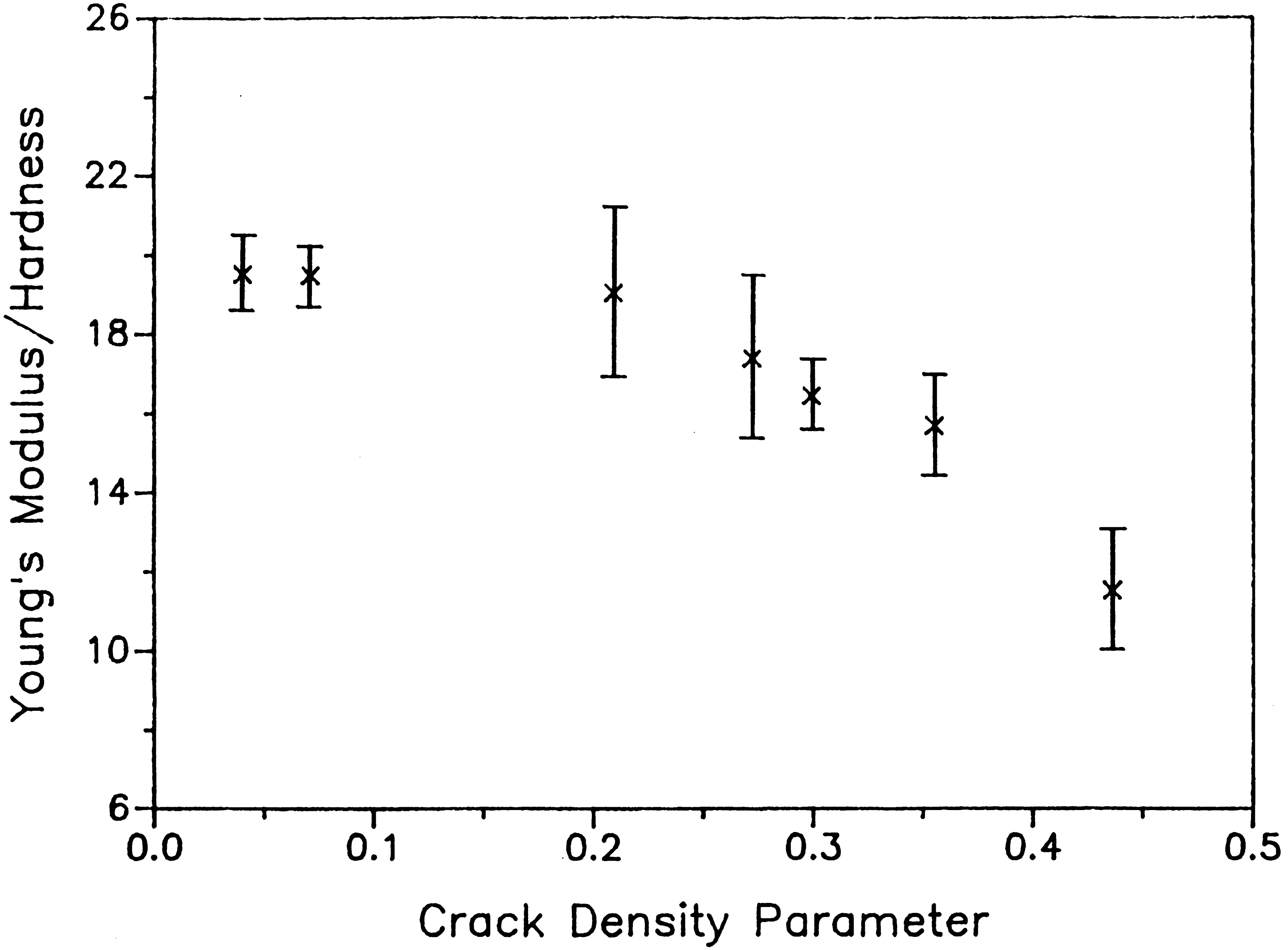

Figure 12 (a). Young's modulus/hardness ratio versus crack density parameter without porosity correction for yttrium chromite. Error bars indicate ± S range where S - standard deviation.

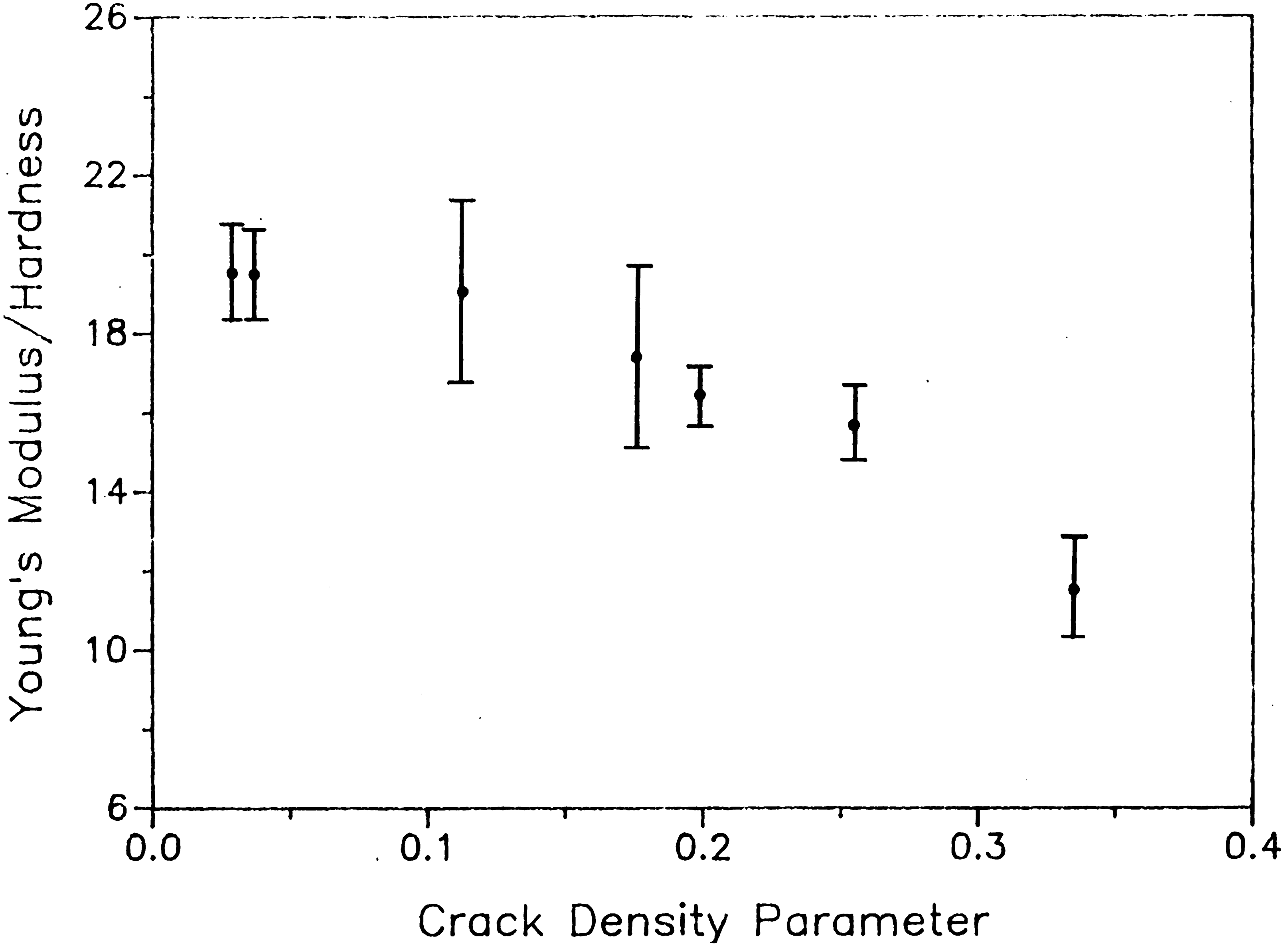

Figure 12 (b). Young's modulus/hardness ratio versus crack density parameter with porosity correction for yttrium chromite. Error bars indicate ± S range where S = standard deviation.

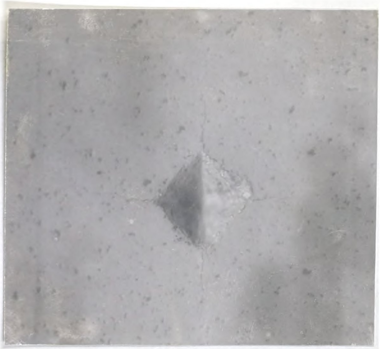

100 microns

Vickers indentation

Yttrium Chromite

Load = 5.88 N

Figure 13. Optical micrograph of yttrium chromite specimen Y0 indented at 5.88N

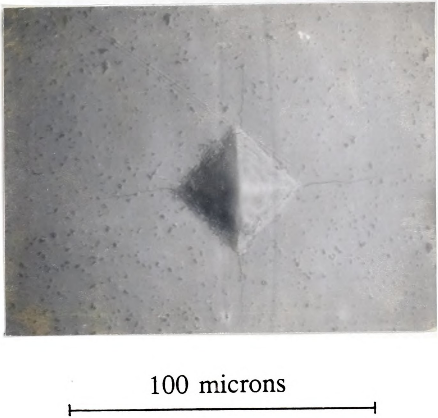

Vickers indentation
Yttrium Chromite
Load = 9.8 N

Figure 14. Optical micrograph of yttrium chromite specimen Y4 indented at 9.8N

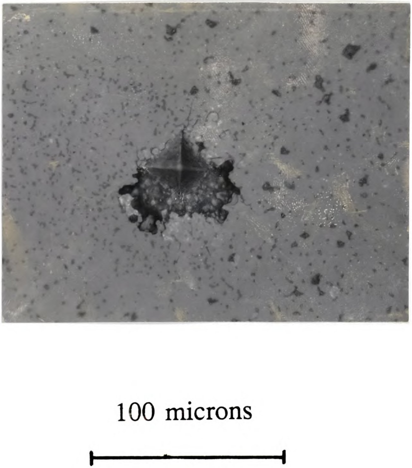

Figure 15. Optical micrograph of yttrium chromite specimen YP21 indented at 4.9N

4.2 Comparison of Fracture Toughness between Experimental Data and Theoretical Equation from 3.3

If we estimate that a is equal to c and that a is the same for all the cracks, we can derive the following equation from equations (8) and (27).

$$\epsilon = N \langle a^3 \rangle \tag{8}$$

$$A = N^{2/3} \langle c^2 \rangle \tag{27}$$

If all cracks have radius a, then <a> = a and

$$A^3 = N^2 a^6 = \epsilon^2$$

$$A = \epsilon^{2/3} \quad . \tag{38}$$

From equations (22), (28) and (38),

$$k = (1 - \epsilon^{2/3})^{1/2} \tag{39}$$

From equation (39), equations (29), (30) and (31) can be written as follows, respectively,

$$K_0/K_c = \frac{(1 - \epsilon^{2/3})^{1/2}}{C} \tag{40}$$

$$K_0/K_c = (1 - \epsilon^{2/3})^{1/2} \tag{41}$$

$$K_0/K_c = 1 - \epsilon^{2/3} \tag{42}$$

Equations (40), (41), (42) and the experimental data are plotted in Figures 16 (a) and (b), and 17 (a) and (b). The fracture toughness of microcracked polycrystalline yttrium chromite specimens generally corresponds to Rose's equation which represents the fracture toughness decrease due to microcrack link-up. The fracture toughness corresponds to Rose's theory of the following equation (see Figure 11 (a) and (b).

$$K_c = E\,(1 - \epsilon^{2/3})^{1/2} + F \qquad (43)$$

where K_c = fracture toughness

ϵ = crack density parameter

E = 1.622 and 1.980 for the crack density parameter without porosity correction and with porosity correction, respectively

F = 0.291 and -0.099 for the crack density parameter without porosity correction and with porosity correction, respectively

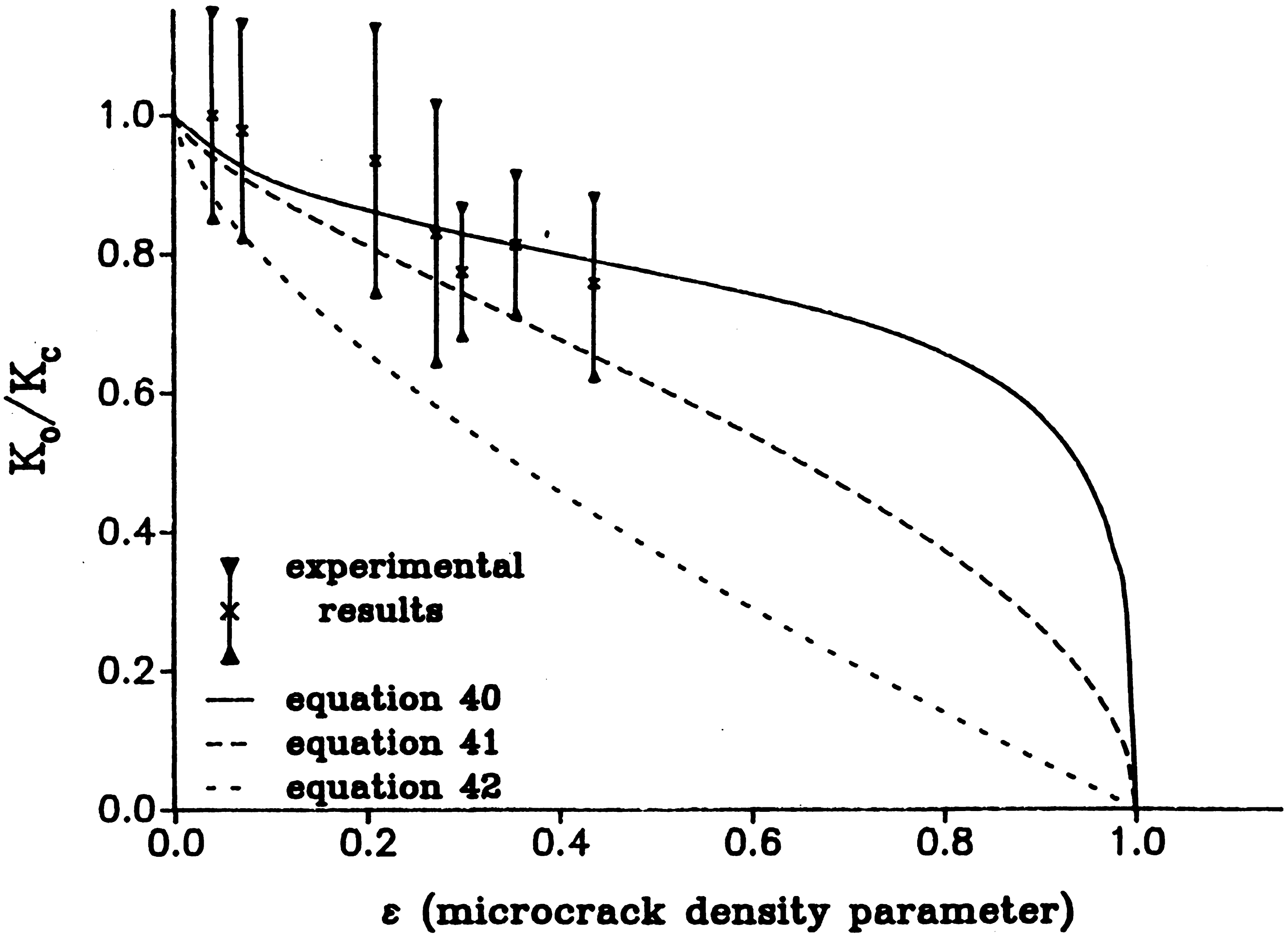

Figure 16 (a). Fracture toughness as a function of microcrack density parameter without porosity correction, ϵ, for the range $0 \leq \epsilon \leq 1$ for three theoretical expressions adapted from Rose (equations (40-42)). Experimental data on yttrium chromite is also included. Error bars indicate ± S where S - standard deviation.

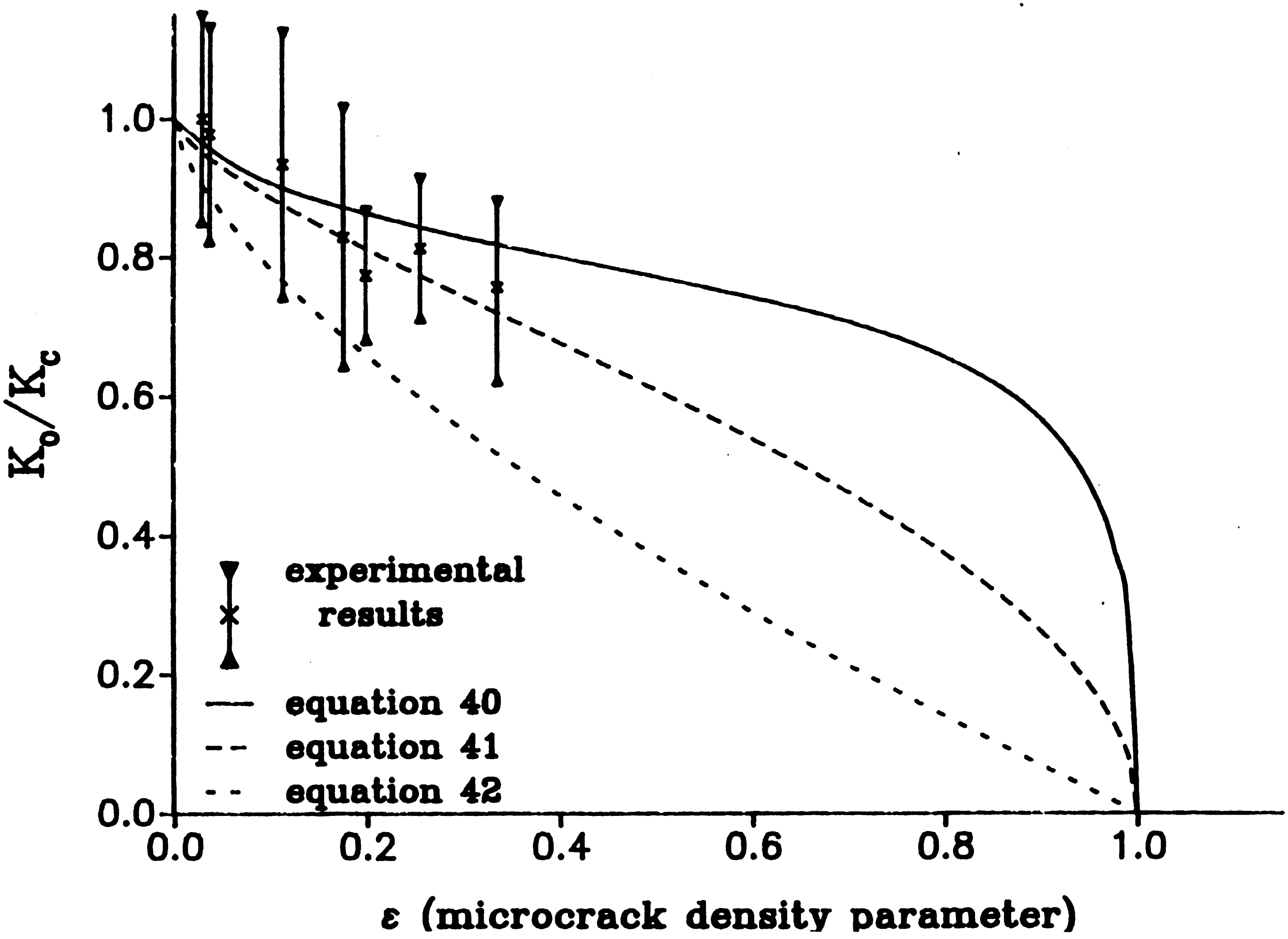

Figure 16 (b). Fracture toughness as a function of microcrack density parameter with porosity correction, ϵ, for the range $0 \leq \epsilon \leq 1$ for three theoretical expressions adapted from Rose (equations (40-42)). Experimental data on yttrium chromite is also included. Error bars indicate ± S where S = standard deviation.

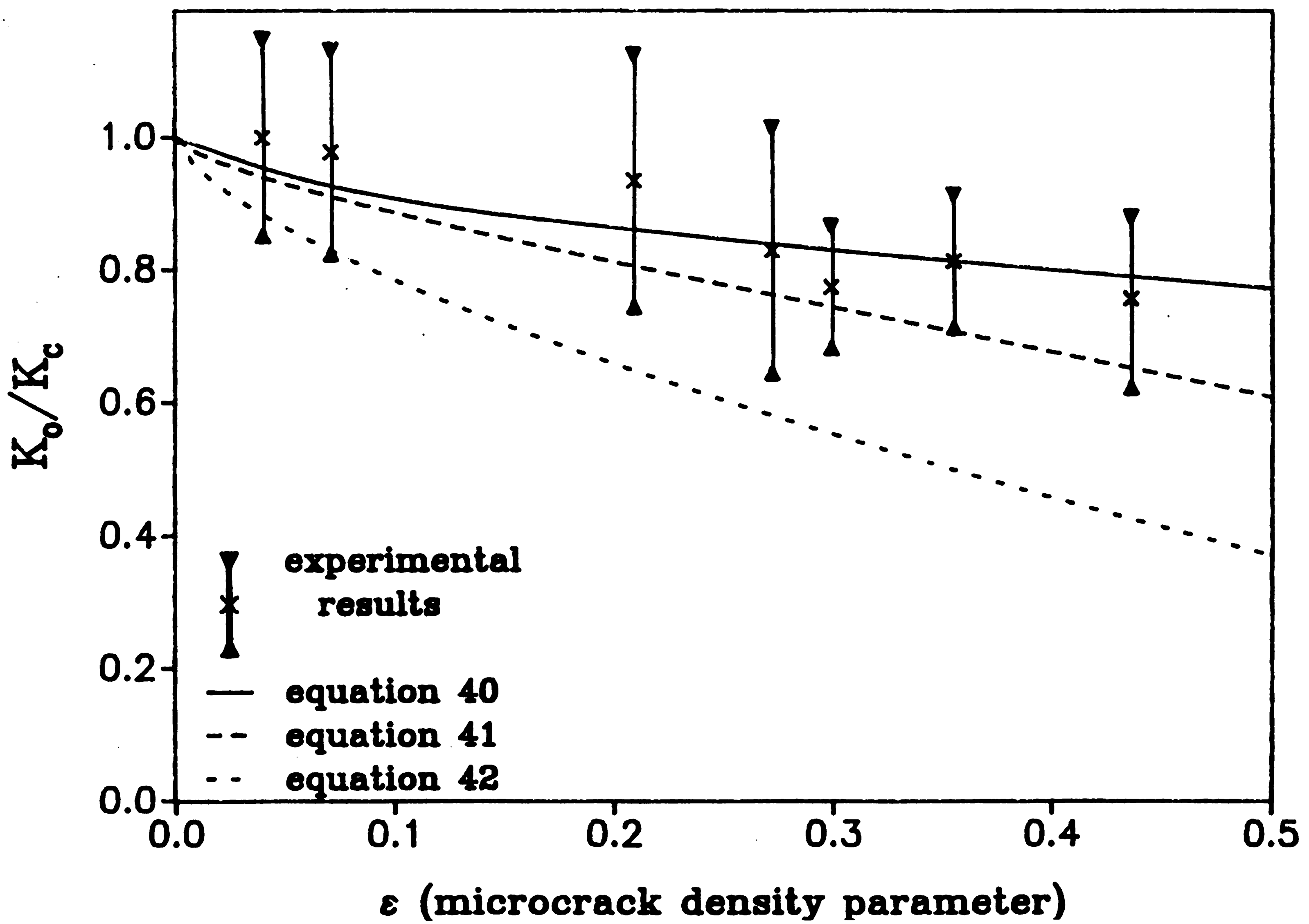

Figure 17 (a). Fracture toughness as a function of microcrack density parameter without porosity correction, ϵ, for the range $0 \leq \epsilon \leq 0.5$ for three theoretical expressions adapted from Rose (equations (40-42)). Experimental data on yttrium chromite is also included. Error bars indicate ± S where S = standard deviation.

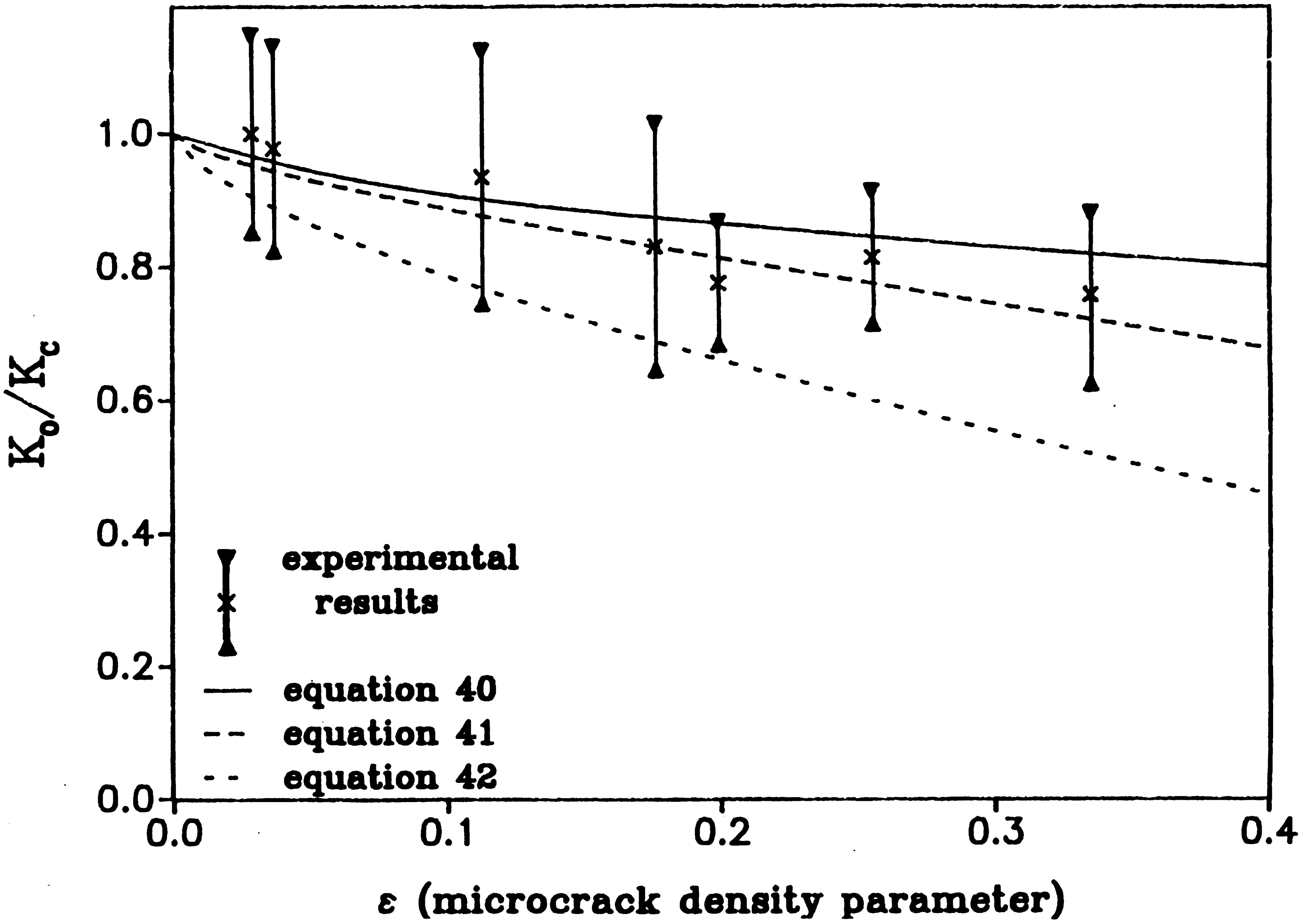

Figure 17 (b). Fracture toughness as a function of microcrack density parameter with porosity correction, ϵ, for the range $0 \leq \epsilon \leq 0.5$ for three theoretical expressions adapted from Rose (equation (40-42)). Experimental data on yttrium chromite is also included. Error bars indicate ± S where S = standard deviation.

5. CONCLUSIONS

Young's modulus, shear modulus and Poisson's ratio were determined by the sonic resonance method for microcracked and nonmicrocracked polycrystalline yttium chromite specimens.

The microcrack density parameter of each specimen was determined using equation (14) and (16) from Poission's ratio and Young's modulus in nonmicrocracked specimens, and the Young's modulus in microcracked specimens. The crack density parameters after porosity correction of the specimens were 0.029, 0.037, 0.113, 0.176 0.199, 0.255 and 0.335.

The hardness was determined from equation (6) using the indentation impression size. The observed decrease in hardness of microcracked polycrystalline yttrium chromite specimen was approximately linear with increasing the crack density parameter over the entire ϵ range. A least-squares fit of the data yielded the relation.

$$H = A - B\epsilon$$

where A = 13.92 and 13.23 for the hardness versus the crack density parameter without porosity correction and with porosity correction, respectively

B = 19.52 and 24.45 for the hardness versus the crack density parameter without porosity correction and with porosity correction, respectively

Fracture toughness was computed from equation (7) using indentation crack size. Fracture toughness decreased linearly with ϵ, the crack density parameter. The relating equation was by a least-square fit

$$K_c = C - D\epsilon$$

where C = 1.853 and 1.815 for the fracture toughness versus ϵ without porosity correction and with porosity correction, respectively

D = 1.177 and 1.498 for the fracture toughness versus ϵ without porosity correction and with porosity correction, respectively

These results imply that pre-existing microcracks in yttrium chromite link-up ahead of a moving macrocrack. Also, the observed trends in fracture toughness is consistant with Rose's theory for microcrack link-up with a moving macrocrack.

The relation between Young's modulus/hardness ratio and crack density parameter was difficult to summarize mathematically. However, Young's modulus/hardness ratio was approximately constant for low values of crack density parameter. In contrast, the Young's modulus/hardness ratio decreased with ϵ for crack density parameter values higher than about 0.2.

6. REFERENCES

1. K. T. Faber, "Toughening of Ceramic Materials", Ph.D. Thesis, University of California, Berkeley, CA (1982).
2. A. G. Evans and K. T. Faber, J. Amer. Ceram. Soc., <u>64</u> [7]: 394-398 (1981).
3. Y. Fu and A. G. Evans, Acta Metall., <u>30</u>: 1619-1625 (1982).
4. F. F. Lange, J. Mater. Science, <u>17</u>: 235-241 (1982).
5. D. L. Porter, A. G. Evans, and A. H. Heuer, Acta Metall., <u>27</u>: 1649-1654 (1979).
6. A. G. Evans and A. H. Heur, J. Amer. Ceram. Soc., <u>63</u> [5-6]: 241-248 (1980).
7. R. C. Garvie, R. R. Hughan and R. T. Pascoe, pp. 263 in "Processing of Crystalline Ceramics," edited by H. Palmour, R. F. Davis and T. M. Hare, Plenum Press, New York (1977).
8. R. C. Garvie, R. H. Hannick and R. T. Pascoe, Nature, <u>258</u>: 703-706 (1975).
9. Y. Ikuma and A. Virkar, J. Mater. Science, <u>19</u>: 2233-2238 (1984).
10. A. G. Evans and R. M. Cannon, Acta Metall., <u>34</u> [5]: 761-800 (1986).
11. J. A. Kuszyk and R. C. Bradt, J. Amer. Ceram. Soc., <u>56</u> [8]: 420-423 (1973).
12. R. W. Davidge and T. J. Green, J. Mater. Science, <u>3</u>: 629-634 (1968).
13. E. D. Case, J. R. Smyth and O. Hunter, Materials Science and Engineering, <u>51</u>: 175-179 (1981).
14. E. Horbogen and K. Friedrich, J. Mater. Science, <u>15</u>: 2175-2182 (1980).

15. R. P. Waki and B. Iluter, J. Mater. Science, 15 [4]: 875-885 (1980).

16. F. F. Lange, Philo. Mag., 22: 983-992 (1970).

17. D. J. Green, P. S. Nicholson and J. D. Embury, J. Mater. Science, 14: 1657-1661 (1979).

18. S. Melin, Int. J. Fracture, 23: 37-45 (1983).

19. E. D. Case and C. J. Glinka, J. Mater. Science, 19: 2962-2968 (1984).

20. W. D. Kingery, H. K. Bowen and D. R. Uhlmann, Chapter 5 in Introduction to Ceramics, Second Edition, John Wiley and Sons, New York (1976).

21. E. D. Case, J. Mater. Science, 19: 3702-3712 (1984).

22. E. D. Case, T. Negas and L. P. Domingues, unpublished data.

23. K. Hardman-Rhyne, N. F. Berk, and E. D. Case, "Porosity Study of Sintered and Green Compact $YCrO_3$ Using Small Angle Neutron Scattering Techniques," pp. 103-108, in Nondestructive Evaluation: Application to Materials Processing, edited by O. Buck and S. M. Wolf, Amer. Soc. for Metals, Metals Park, Ohio (1984).

24. T. Negas and L. P. Dominges, in "Fourth International Meeting on Modern Ceramics", edited by P. Vincenzini (Elsevier Interscience, New York, pp. 993 (1979).

25. R. L. Fullman, AIME Trans., 1973: 447-452 (1953).

26. E. D. Case, J. R. Smyth and V. Monthei, Commun. J. Amer. Ceram. Soc., 64: c24-c25 (1981).

27. F. Forster, Z. Metall, 29: 109-115 (1937).

28. S. Spinner and W. E. Tefft, ASTM Proc., 61: 1221-1238 (1961).

29. H. R. Kase, J. A. Tesk and E. D. Case, J. Mater. Science, 20: 524-531 (1985).

30. G. Picket, ASTM Proc., 45: 846-865 (1945).

31. B. R. Lawn and D. B. Marshall, J. Amer. Ceram. Soc., 62 [7-8]: 347-350 (1979).

32. G. R. Antis, P. Chantikul, B. R. Lawn and D. B. Marshall, J. Amer. Ceram. Soc., 64 [9]: 533-538 (1981).

33. B. R. Lawn and M. V. Swain, J. Mater. Science. 10 [1]: 113-122 (1975).

34. B. R. Lawn, A. G. Evans and D. B. Marshall, J. Amer. Ceram. Soc., 63 [9-10]: 574-581 (1980).

35. J. B. Walsh, J. Geophysical Research, 70 [20]: 5249-5257 (1965).

36. R. L. Salganik, Mechanics of Solids, 8 [4]: 135-143 (1973); English Translation.

37. B. Budiansky and R. L. O'Connell, Int. J. Solids Structures, 12: 81-92 (1976).

38. D. P. H. Hasselman and J. P. Singh, Ceram. Bull., 58: 856-860 (1979).

39. J. Kemeny and N. G. W. Cook, Int. J. Rock Mech. Min. Sci., 23 [2]: 107-118 (1986).

40. J. B. Walsh, J. Geophys. Res., 70: 399-411 (1965).

41. G. R. Irwin, J. Appl. Mech., 24: 361-364 (1957).

42. J. R. Rice, Mathematical Analysis in the Mechanics of Fracture, pp. 191- 311, Fracture, Vol 2 (edited by H. Libowitz) Academic Press, New York (1968).

43. E. D. Case, J. R. Smyth and O. Hunter, J. Mat. Sci., 15: 149-153 (1980).

44. A. G. Evans, Acta Metall., 26: 1845-1853 (1978).

45. Y. Fu , A. G. Evans and W. M. Kriven, J. Amer. Ceram. Soc., 67 [9]: 626-630 (1984).

46. L. R. F. Rose, J. Amer. Ceram. Soc., 69 [3]: 212-214 (1986).

47. W. Kreher and W. Pompe, J. Mater. Science, 16: 694-706 (1981).

48. A. G. Evans and K. T. Faber, J. Amer. Ceram. Soc., 67 [4]: 255-260 (1984).

49. J. K. Mackenzie, Proc. Phys. Soc. (Lond.), 63B: 2-11 (1950).

APPENDIX 1. Derivation of Equation (12) in Section 3.1

From equation (10) and (11) in Section 3.1 of this thesis,

$$U_e = \frac{(1 - \nu_0^2)}{Y} \int_0^c \left[\frac{4}{\pi^2} \sigma^2 \sin^4\gamma(\pi c) + \frac{16}{\pi^2(2 - \nu_0)^2} \sigma^2 \sin^2\gamma \cos^2\gamma \cos^2\omega \right.$$

$$\left. (\pi c) + \frac{16\,(1 - \nu_0)^2}{\pi^2\,(2 - \nu_0)^2(1 - \nu_0)} \sigma^2 \sin^2\gamma \cos^2\gamma \sin^2\omega\,(\pi c) \right] 2\pi c dc \qquad (44)$$

If we use the relations of $\langle \sin\omega^2 \rangle = \langle \cos\omega^2 \rangle = 1/2$, $\langle \sin\gamma^4 \rangle = 1/5$ and $\langle \sin\gamma^2 \cos\gamma^2 \rangle = 2/15$, then equation (44) can be rewritten as

$$U_e = \frac{8}{3Y} (1 - \nu_0^2)\sigma^2 c^3 \left[\sin^4\gamma + \frac{4}{(2 - \nu_0)^2} \sin^2\gamma \cos^2\gamma \cos^2\omega \right.$$

$$\left. + \frac{4}{(2 - \nu_0)^2} (1 - \nu_0)\sin\gamma^2 \cos\gamma^2 \sin^2\omega \right]$$

$$= \frac{8}{45Y} (1 - \nu_0^2)\sigma^2 c^3 \left[3 + 4/(2 - \nu_0)^2 + 4\,(1 - \nu_0)/(2 - \nu_0)^2\right]$$

$$= \frac{8}{45Y} \sigma^2 c^3 (1 - \nu_0^2) \frac{10 - 3\nu_0}{2 - \nu_0} \qquad (45)$$

If it is assumed that there are N penny-shaped cracks with mean crack radius cubed $\langle c^3 \rangle$ in the body, equation (45) becomes

$$U_e = \frac{8}{45Y} N\sigma^2 \langle c \rangle^3 (1 - \nu_0^2) \frac{10 - 3\nu_0}{2 - \nu_0}$$

which is identical to equation (12) in Section 3.1 of this thesis.

APPENDIX 2. Rule of Mixtures Relations

Based on the assumption that "the reduction in load-bearing area" will reduce fracture toughness via microcracking, Evans and Faber gave [2]

$$\Gamma_0 = \Gamma_c (1 - V_m) \tag{46a}$$

where Γ_0 = the intrinsic resistance to crack of microcracked body

Γ_c = the matrix toughness

V_m = volume fraction of microcracks

Evans and Faber [2] also give the following relations between crack toughness and elastic modulus

$$K_c^2 = E_c \Gamma_c \tag{47}$$

$$K_0^2 = E_0 \Gamma_0 \tag{48}$$

where K_c = the intrinsic fracture toughness of the nonmicrocracked body

K_0 = the effective fracture toughness of the microcracked body

E_c = Young's modulus of the nonmicrocracked body

E_0 = Young's modulus of the microcracked body

Substituting equations (47) and (48) into equation (46a) gives

$$K_0^2 = K_c^2 (E_0/E_c)\ (1 - V_m) \qquad (46b)$$

Taking the square root of equation (46b) and assuming $E_0 = E_c$, then for dilute crack systems,

$$K_0 = K_c\ (1 - V_m)^{1/2} \qquad (49)$$

If we assume the volume fraction of microcracks, $V_m = A$, the area fraction of the fracture plane corresponding to pre-existing microcracks, and use equation (38), then equation (49) gives

$$K_0\ /K_c = (1 - \epsilon^{2/3})^{1/2} \qquad (41)$$

Rose refers to this equation as being based on a "rule of mixture for the work of fracture."

If the reduction of fracture toughness in the presence of microcracks is based on a rule of mixtures for fracture toughness K_0 and K_c (assuming V_m<<1) [10, 48], we can obtain the following equation.

$$K_0 = K_c\ (1 - V_m\ ) \qquad (50)$$

If we also assume $V_m = A$, the area fraction of the fracture plane corresponding to pre-existing microcracks, and use equation (38), equation (50), then we obtain

$$K_0 = 1 - \epsilon^{2/3} \qquad (42)$$

Rose indicated that equation (42) of rule of mixture, "underestimate the interaction between main crack and microcrack, and consequently should overestimate the effective toughness." However, Rose indicated that equation (42) will be correct for K_0, "if the linking-up occurred quasi-statically." Rose mentioned that " K_c should be taken to be $\bar{K}_c$ because a reduction in effective modulus due to a homogeneous distribution of microcracks should be compensated for a reduction in the effective K_c."

$$\bar{K}_c = (\bar{E}/E)^{1/2} K_c \tag{51}$$

where $\bar{K}_c$ = the effective fracture toughness for the homogeneously microcracked material

K_c = the intrinsic fracture toughness for the material without microcracks

$\bar{E}$ = the effective Young's modulus for the homogeneously microcracked material

E = the intrinsic Young's modulus for the material without microcracks